Modeling and optimization of electro-optic materials used in Mach-Zehnder optical switches

by

Arya Fatehi

Master of Engineering

Department of Electrical and Computer Engineering

McGill University

Montreal,Quebec

June 2011

A Thesis Submitted to the
Faculty of Graduate Studies and Research
In Partial Fulfillment of Requirements for the Degree of
Master of Engineering

ABSTRACT

New information technologies demand flexible optical networks. Optical space switches offer efficient transmission capacity useful for those applications. High bandwidth and low drive voltage modulation are advantages of the optical space switches. The objective of this research is to optimize the doping profile in the waveguide to maximize the electro-optic effect while at the same time minimizing the optical losses. Double heterostructure semiconductor waveguides was used for optical switch devices. The best combination of the extinction ratio, power efficiency and overall switch dimensions was found in an optical switch with the 10^{18}cm^{-3}-doped $Al_{0.06}Ga_{0.94}As$-upper-cladding, 10^{15}cm^{-3} - doped $GaAs$ - core and 10^{18}cm^{-3} - doped $Al_{0.06}Ga_{0.94}As$-lower-cladding. Devices with claddings made of aluminum gallium arsenide with higher aluminum contents were found to lack the extinction ratios needed for telecommunication switching applications.

ABRÉGÉ

Les nouvelles technologies demandent des réseaux optiques flexibles. Les commutateurs optiques offrent une capacité de transmission efficace et utile pour ces applications. La large bande passante et le faible voltage de modulation sont les avantages des commutateurs optiques en espace. L'objectif de cette recherche est d'optimiser le profil de dopage dans le guide afin de maximiser l'effet d'électro-optique tout en minimisant les pertes optiques. Les guides d'ondes semi-conducteurs à hétérostructure double ont été utilisés pour les appareils de commutation optique. La meilleure combinaison du ratio d'extinction, d'efficacité de puissance et des dimensions globales des commutateurs a été trouvée dans un commutateur optique avec le dessus-revêtement (10^{18}cm^{-3}-dopé $Al_{0.06}Ga_{0.94}As$), le guide d'onde (10^{15}cm^{-3}-$GaAs$ dopé) et le dessous-revêtement (10^{18}cm^{-3}-$Al_{0.06}Ga_{0.94}As$ dopé). Les appareils avec des revêtement en arséniure de gallium aluminium avec des teneurs en hautes aluminium n'ont pas des ratios d'extinction nécessaires pour les applications de commutation des télécommunications.

ACKNOWLEDGEMENTS

I am truly indebted to my thesis supervisor, Professor Andrew Kirk for his guidance, patience and inspiration. His broad knowledge, constant instructions and admirable personality have greatly helped me throughout this work.

I would like to thank all my friends in the McGill's photonic systems group for all the good moments. I am especially grateful to Mr. Chris Rolston for his technical supports. I would also like to thank Professor Ishiang Shih for his valuable discussions.

Last but not least, I would like to express my love and gratitude to my beloved family.

TABLE OF CONTENTS

LIST OF TABLES

LIST OF FIGURES

CHAPTER 1
Introduction

Optical networks rely on wavelength division multiplexed (WDM) networks based on optical add/and drop multiplexers (OADMs) and optical cross-connects (OXCs) for routing the WDM signals. For the device to be compatible with technological advances, several requirements must be met including very low crosstalk values, low-Insertion losses, polarization and wavelength independence, and a high switching speed [1]. Using the optical switches in these devices can improve the node performance by increasing the throughput, decreasing the size, power consumption, heat dissipation and cost [2-3]. Figure 1-1 shows a schematic of a 4×4 optical switch capable of connecting each of input ports to any output port. The physical properties and processing flexibility of III-V semiconductors make them suitable candidates for guided wave devices.

Typically, double heterostructure semiconductor waveguides are used for optical switch devices [4]. In these structures, optical confinement is obtained by compositional change, so the optical and electrical waveguide structure can be optimized separately. These waveguide structures are generated using a combination of epitaxial growth with processing techniques such as localized etching. In the semiconductor waveguides, the index of refraction as well as the absorption/gain can be modulated. The modulation of the former is carried out either by applying an electric field or

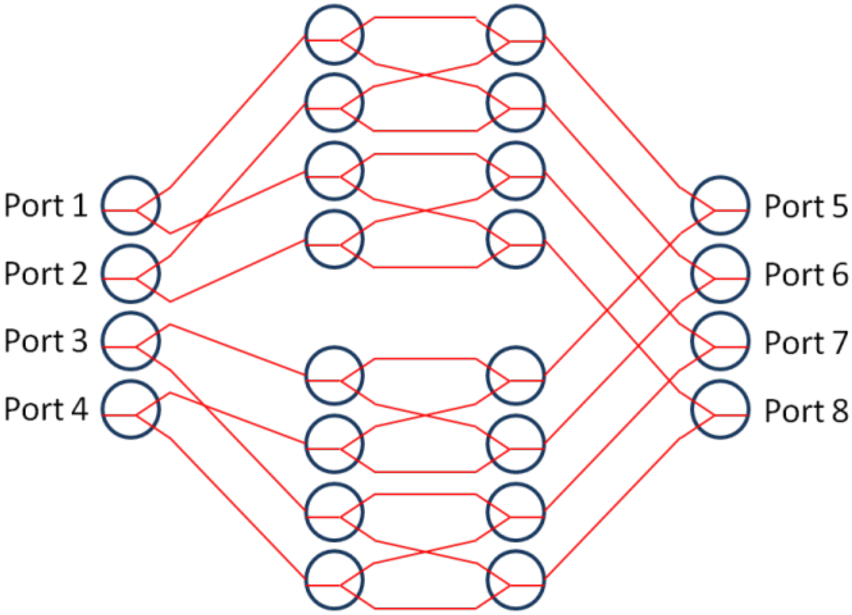

Figure 1–1: A 4×4 optical space division switch

injecting the carriers. The change in the index of refraction is usually greater by free carrier injection than the electro-optic (E-O) effect (up to two orders of magnitude [4]). However, the speed of the device is determined by the carrier recombination time, which makes the device generally slower than those that use the E-O effect. Also, the E-O and carrier injection modulation can be combined by doping the ($AlGaAs$) core. In this case, the speed is determined by the device capacitance rather than the carrier recombination rate. Moreover, a need exists for very low resistance between the cladding layers and the metal contact. Resistance at the Ohmic contact is detrimental to the device, leading to the breakage of the electric field at the interface. This phenomenon can be avoided by wisely selecting the metal alloy, and highly doping the $GaAs$ top layer, which reduces the barrier height.

The objective of this research is to optimize the doping profile in the waveguide so to maximize the E-O effect while at the same time minimizing the optical losses. Chapter 2 describes the conventional modulating methods used to modify the index of refraction of various materials. In addition, Chapter 2 also describes the materials, and their properties, that are extensively used in optical switching. Chapter 3 mainly concentrates on the E-O effect and the parameters that influence its magnitude. In addition, this chapter describes the effects of doping on the electro-optic behavior of a material, as well as band filling and plasma effect, and bandgap shrinkage. Chapter 4 provides a simulation of the refractive index change in various heterostructures. Finally, Chapter 5 describes the design of Mach-Zehnder interferometric optical switches.

CHAPTER 2
Optical Switches: A Literature Review

In this chapter, conventional optical modulation methods are described. In addition, the key optical switching devices are presented and finally the properties of lithium niobate, III-V compound semiconductors, and optical polymers are reviewed.

2.1 Optical Modulation Methods

Modifying the refractive index of materials can be achieved by several methods, three of which will be described in this section.

2.1.1 Thermo-Optic Modulation

The functionality of thermo-optic (T-O) switches is based on modulating the refractive index of material through changing temperature. The change in the refractive index arises from a change in electronic polarizability and density [5].

The main restriction of these switches, however, is the opposite relationship between their speed and power efficiency. Faster switches tend to dissipate the heat more quickly and hence require a constant generation of heat to remain in certain states. On the other hand, a switch made of a low thermal conductivity material retains heat more efficiently, although this type of switch suffers from low speeds. In addition, since electrical micro-heaters are generally used in T-O switches, the speed of these switches is controlled by the electrical-thermal conversion and diffusion time [2].

The typical materials for T-O switching are polymers, silica waveguides, and silicon-on-insulator (SOI). Although silica waveguides have T-O coefficients approximately of an order of magnitude less than those of polymers, the thermal conductivity of silica waveguides can be ten times larger. Hence, depending on the design, either can be employed: polymers can be used in a device with requirements for a large index contrast, and silica can be used in a device that demands small index changes and therefore faster switching [6].

2.1.2 Electro-Optic Modulation

The application of an electric field to noncentrosymmetric crystals can change their refractive index by modifying the position and/or density of the charge carriers and by inducing slight deformations in the ion lattice. This phenomenon is referred to as the electro-optic (E-O) effect, which will be discussed exhaustively in chapter 4. Linear E-O coefficients lead to a maximum refractive index modulation of about ±0.001 (limited by the breakdown voltage of the material), which is one order of magnitude less than T-O effects. Nonetheless, since E-O effects are very fast (as opposed to T-O effects), they can achieve switching times of less than a nanosecond [7].

2.1.3 Current Injection

Tuning a semiconductor optical filter by electrical current injection is considered as an alternative solution with tuning speeds on the order of nanoseconds (limited by the carrier lifetime in the material). Electrical current injection has been also successfully used for tuning an arrayed waveguide grating by controlling the phase of individual waveguides [8].

2.2 Types of Optical Switches

There are many different ways in which a change in refractive index can be used to physically change the propagation path of a lightwave, and that different switch architectures have been introduced to accomplish this. The most widespread switch architectures will be explained in this section.

2.2.1 Directional Coupler

Directional couplers (DC) consist of two waveguides with a small separation between them (Figure 2-1). DCs are characterized by their coupling length (L_c) and the bias voltage or current needed to achieve a π-phase-shift in the interferometer. In the case of two identical waveguides, optical power can be transferred to the other waveguide in its entirety after traveling a certain distance-the coupling length $L_c = \frac{\pi}{2}\kappa$ [2]. DCs require small index changes typically caused by a switching voltage of only 11V for a 2-mm-long E-O switching device.

If the light propagates into one waveguide with a proximity region equal to the coupling length L_c, it will be coupled into the other waveguide (cross state). On the

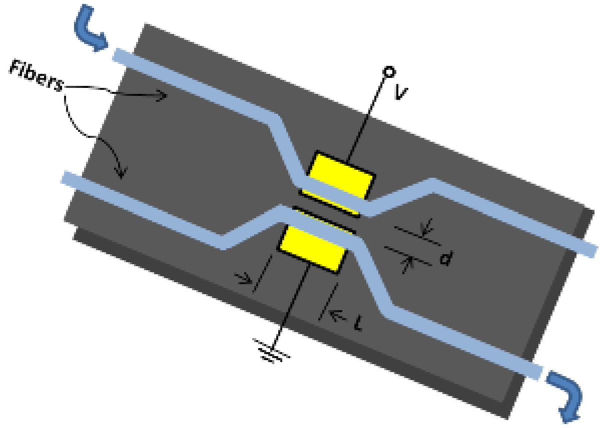

Figure 2–1: A schematic of a directional coupler

other hand, if the light travels a distance twice as long as the coupling length, the power transfers back to the original waveguide (bar state). If the voltage is applied across one waveguide, the resulting refractive index difference reduces the coupling between the waveguides. When the change in the refractive index reaches a certain value, the coupling is minimized, and optical power remains in the same waveguide (bar state)[2].

The coupling coefficient is defined as follows:

$$\kappa = \kappa_0 exp(-\gamma g) \tag{2.1}$$

where g is the waveguide separation, and κ_0 and γ are constants. κ depends on the propagation distance and the waveguide separation [2]. Directional coupler switches are polarization dependent for two reasons; 1) the coupling length is usually different for TE and TM modes and 2) the E-O effect used for the refractive-index changes can be polarization dependent.

2.2.2 Fabry-Perot (FP) Switches

Typically, FP filters comprise two partially reflecting mirrors with a small gap between them where the light incident to the filter can undergo multiple reflections. When the optical path length of the cavity between the mirrors is an even multiple of the light half-wavelength, the light is transmitted through the cavity. In the event that the optical length is an odd multiple of the light half-wavelength, the light is reflected.

A change in the refractive index is a way to tune FP cavities. A schematic of the possible optical space switch based on the FP filter is illustrated in Figure 2-2 [6]. A change in the voltage causes the transmission or reflection of the incident beam. Despite being very fast, an FP filter is not a complete replacement for Micro-electromechanical systems (MEMS), since its refractive index modulation is relatively small. The tuning of the wavelength response of FP cavities is no more than 1nm by the E-O effect method. Nonetheless, in FP cavities, the bandwidth can be extended by decreasing the free spectral range (FSR) to create a comb response, which transmits or reflects one out of every two channels of the grid targeted for the switch. Therefore, any channels covered by the comb response can be redirected by the tuning of the FP cavity response by an equivalent of one channel spacing. To increase the passband width, multiple high-order FP cavities are coupled to form a comb filter [9].

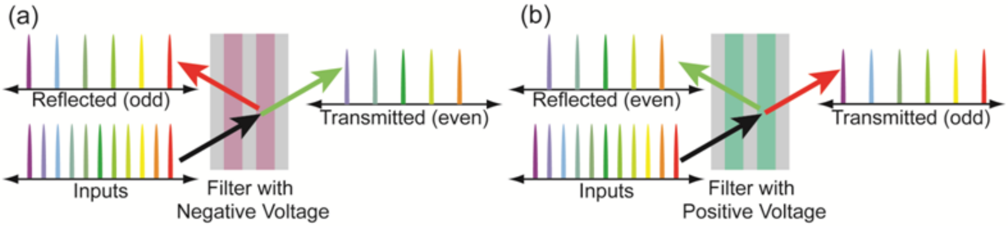

Figure 2–2: Illustration of an E-O comb Fabry-Perot switch response when a) a negative voltage and b) a positive voltage is applied [10]. Comb represents the wavelengths.

In optical telecommunications, FP filters are commonly used as wavelength-selective filters to isolate channels. Moreover, FP filters can be utilized as switchable reflectors capable of reflecting or transmitting light similar to micro-electro-mechanical system (MEMS) mirrors [10].

By altering the refractive index of mirrors through the E-O effect, the transmission or reflection of incident light in FP mirrors can be fine-tuned. The FP cavity can be made of semiconductors, ferroelectric, or liquid crystal materials; and the refractive index of the cavity can be modulated through E-O, T-O, piezoelectric, or all optical effects [6].

2.2.3 MachZehnder Interferometric Switches

The Mach-Zehnder interferometer (MZI) incorporates a 3 dB coupler that can split the incoming light into two decoupled waveguides. Then, the light finds its way through a phase tuning section of length L in one of the waveguides, followed by a second 3 dB couple as an output combiner. The signal in the tuning section is modified to have either constructive or destructive interference with the other signal at the second 3 dB coupler, and the combined output signal is routed to the cross or the bar port depending on the phase change (Figure 2-3) [2].

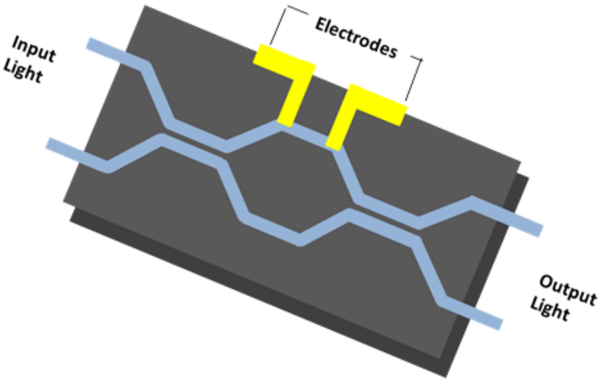

Figure 2–3: A schematic of Mach-Zehnder interferometric optical switch.

This kind of device is designed by connecting directional couplers with length $L_c/2$ (3-dB coupler). In this case, the total index change required for switching is smaller compared to that of the directional coupler. At the phase shifter, the symmetric modes undergo a transition to modes. A $\pi/2$ phase difference exists between the modes at the end of the input 3-dB coupler. At the output 3-dB coupler, the phase difference reaches π, which leads to the cross state. A wide waveguide gap may result in a reduction in coupling between the waveguides (equation 2.1).

The transmission characteristics can be calculated as follows [2]:

$$\frac{P_{out}}{P_{in}} = \cos^2 \frac{\Delta\beta L}{2} ....(cross) \tag{2.2}$$

$$\frac{P_{out}}{P_{in}} = \sin^2 \frac{\Delta\beta L}{2} ....(bar) \tag{2.3}$$

where $L = L_c/2$ for 3-dB splitting, $\Delta\varphi = L\Delta\beta$, L is the length of the phase tuning section, and $\Delta\beta$ is the change in the propagation constant. A phase change of only $L\Delta\beta = \pi$ is required for switching operation, which is $\sqrt{3}$ times smaller than that of the directional coupler. MZIs are well suited for high-speed application, since the E-O field effects can be exploited. Traveling-wave electrodes integrated on bulk $InGaAsP$-InP MZI switches allow a bandwidth of 35 GHz [49]. The MZI-based T-O switches are wavelength and polarization dependent, which is due to birefringence.

2.2.4 Other Types of Switches

Micro-electromechanical systems (MEMS) are most commonly actualized as moveable micro-mirrors. Electrostatic actuation is the prominent mechanism used in these devices. Electrostatic forces are created between conductors with different electric potentials. A MEMS mirror can be adjusted by varying the applied voltage across the electrodes. MEMS, although extensively used, need a mechanical movement to modify the light direction. As a result, MEMS switches have response times between 10 μs and 10 ms [5], which are limited by the mechanical resonance frequency [11]. Some advantages of MEMS mirrors are that they are broadband, and if the beam is properly collimated, they can be low loss with limited crosstalk [10].

Another type of optical switch is a resonator-based switch, which is most similar to an integrated Fabry-Perot optical space switch.

2.3 Common Materials for Optical Switching

In this section, the most used materials in optical switching industry will be described briefly.

2.3.1 Lithium Niobate

The most frequently used E-O material is lithium niobate ($LiNbO_3$) due to its high E-O coefficient (r_{33} of 30.8). One of the advantages of this material is its ability to form low loss planar waveguides through titanium diffusion or proton exchange [2, 10]. $LiNbO_3$ (or LN) is a ferroelectric crystal that posses electric dipoles even in the absence of an electric field. Above a certain temperature, called the Curie temperature, the ferroelectric effect disappears. $LiNbO_3$ generally demonstrates the Pockels effect, which will be discussed later in section 4.1.1.

Depending on the composition of the E-O material, the Curie temperature varies within the 1120-1210°C range, and the melting point of the E-O material varies within the 1150-1250°C range. Due to the anisotropic nature of the crystal, the refractive index for light polarized along the c-axis is smaller than the refractive index for light polarized perpendicular to this axis. Composition, temperature, and wavelength have stronger effects on the refractive index in the directions normal to the c-axis than those parallel to it. The typical refractive index values are 2.21 and 2.14 at 1.55 μm wavelength for directions normal and parallel to the c-axis (Figure 2-4), respectively [2].

The advantages of LN are zero chirp, very low insertion loss, and very a large E-O coefficient [13]. The devices based on this material also benefit from an absence

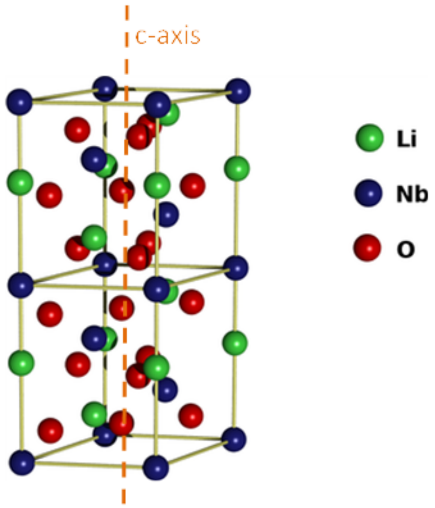

Figure 2–4: Hexagonal crystal structure of $LiNbO_3$ [12].

of moving parts, low power consumption, and very fast switching speeds (switching times down to tens of nanoseconds). The applications of LN for fast switching are optical packet switching, optical burst switching, fast (de)multiplexing of ultra-high-capacity optical signals, and fast and flexible optical cross-connects of small scale. Nevertheless, size limitations (maximum 16×16 or 32×32) are one of the issues that limit the usage of LN.

Other ferroelectric materials used in optical switches are lead zirconate titanate-$Pb(Zr, Ti)O_3$ or PZT- and lead lanthaunum zirconate titanate-$(Pb, La)(Zr, Ti)O_3$, or PLZT [14].

2.3.2 Compound Semiconductors

Unlike silicon, compound semiconductors possess an E-O coefficient. In spite of their relatively small E-O coefficients, compound semiconductors can obtain index modulations of the same order as $LiNbO_3$ due to the high refractive index of the semiconductors. The E-O index change is proportional to the cubic power of the refractive index; thus, the high refractive index compensates for the low E-O coefficient. Furthermore, low index dispersion makes the electrical signal travel faster than the optical signal. Optical confinement also can be better achieved in a material with a high refractive index [13].

In III-V semiconductors, the E-O effect is typically obtained with a p-i-n structure that is reverse biased [13]. The application of an electric field alters the depletion region width, which results in a modification of the refractive index due to electro-optic, band filling, Franz-Keldysh, and plasma effects when the incident wavelength is far from the absorption edge of the material [15]. For III-V semiconductors to benefit from the premium performance, nearly perfect interfaces are considered indispensable. Today, high demands on growth characteristics can be met by processes such as molecular beam epitaxy (MBE) and metalorganic chemical vapor deposition (MOCVD) [16].

The requirements for the semiconductors used in epitaxial layers are as follows [16]:

1. Two materials must have the same crystal structure (or at least symmetry). Usually, this requirement is met by the common III-V compounds.
2. The two lattice constants must be almost identical.

The lattice constant of an alloy can be calculated based on the linear interpolation between its constituents. For $Al_xGa_{1-x}As$, one can obtain the following:

$$a_{AlGaAs} = xa_{AlAs} + (1-x)a_{GaAs} \tag{2.4}$$

Figure 2-5 illustrates the lattice constant variations of different alloy compositions. In $InAlGaAs$, the lattice constant variations with fraction x are merely less than 0.15%. As a result, it is possible to grow layers of $GaAs$ and $AlAs$ or any of the intermediate alloys on top of one another without generating an undesirable stress. However, few materials exist that can be grown on a $GaAs$ substrate without introducing strain. As an alternative, InP can be considered for use as a substrate. $Al_{0.48}In_{0.52}As$, $Ga_{0.47}In_{0.53}As$, and $Ga_{0.47}In_{0.53}As$ have the same lattice constants as InP with a direct bandgap, and therefore, they can trap carriers more effectively. Thus, these materials are appealing for high-speed electronic device applications [2].

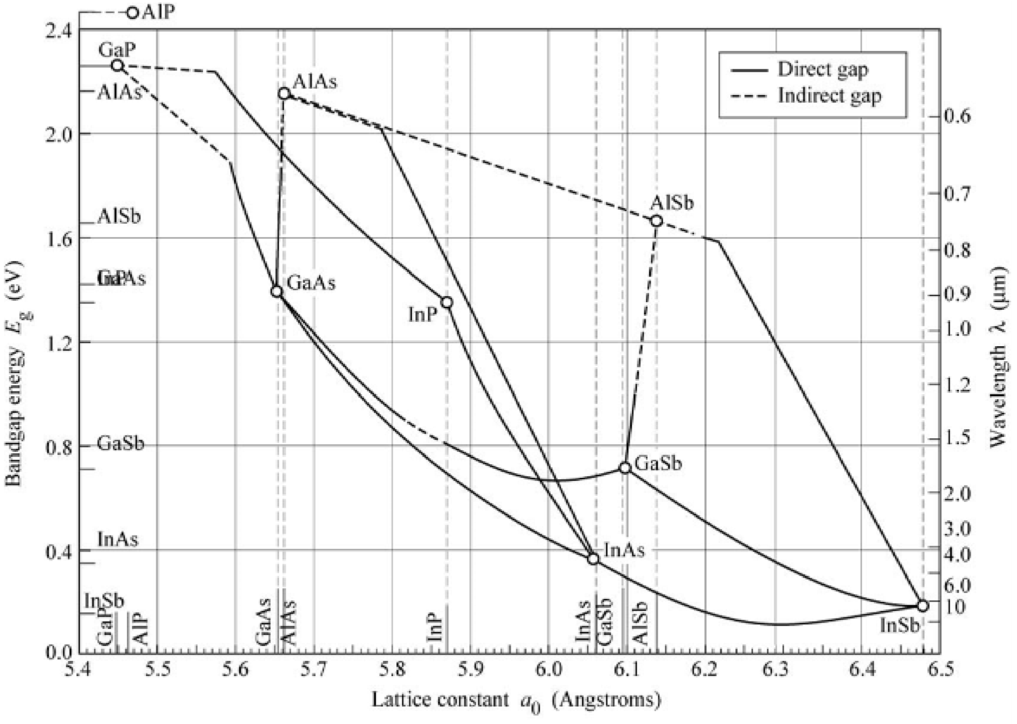

Figure 2–5: The lattice constant and bandgap energy of different III-V compounds [17].

Compound semiconductors are extensively used in optical switches. The refractive index can be controlled with two prominent methods: applying an external electric field or injecting carriers (electrons or holes) into the waveguide layer. The insertion loss is somewhat higher in these materials compared to $LiNbO_3$. On the other hand, silicon lacks the Pockels effect, making carrier injection the only viable method to control the refractive index [2].

2.3.3 Polymers

Electro-optic (E-O) polymers have been the subject of much attention as options for high-speed (wide bandwidth), low-drive-voltage (V_π) electro-optic modulators. The modulators encode an electrical driving signal onto an optical transmission beam.

The nonlinear optical properties of materials can be used to control the phase, the state of polarization, or the frequency of light beams. Other applications of the nonlinear optical properties of materials are for optically storing and restoring information or deflecting light beams and routing optical information between fiber-optic channels [18].

E-O polymers have various advantages over crystalline materials (e.g., lithium niobate) such as the following [19]:

1- Closely matched optical and millimetre wave refractive indices and low-loss tangents that are non-dispersive up to >250 GHz

2- High E-O activity (r_{33})

3- Low dielectric constant for dense devices arrays

4- Property tunability

5- Radiation resistance for space applications

Another important feature of polymers is the tunability of their refractive index, which can have values up to 35%, enabling high-density compact waveguiding structures with small radii of curvature. The negative thermo-optic coefficient ($dn/dT = -1 - 4 \times 10^{-4}$) is 10^{-40} times larger than that of more conventional optical materials, e.g., glass, which helps to reduce power-consumption in thermally-actuated optical elements [20]. The unique properties of polymers are discussed in more detail in the following sections.

2.3.3.1 Glass Transition Temperature (T_g)

The T_g is a temperature above which polymer becomes rubbery. When the chromophore-bearing polymer is subjected to a large electric field at or above the T_g, the interaction of the dipole with the field makes the dipolar species reorient towards the direction of the applied field. If the polymer is then cooled down to the glassy state with the electric field applied, the field-induced non-centrosymmetric orientation becomes frozen, leaving behind a material with a second order optical nonlinearity. The refractive index of such poled material can change when an external electric field is applied [18].

2.3.3.2 Poling

Poling is a pre-requisite processing used to obtain a second order optical nonlinearity in a guest-host E-O polymer system. During this process, an electric field caused by DC voltage is applied at a temperature in the vicinity of the T_g followed by a cooling down, which creates a uniform statistical polar orientation of chromophores. To the first order approximation, the strength of the resultant E-O coefficient and the strength of the applied poling electric field are directly proportional. Therefore, the higher electric fields are preferred before the onset of dielectric breakdown [21].

2.3.3.3 Properties of Optical Polymers

In this section, various properties of polymers will be described briefly.

Refractive Index

The refractive index of a material depends on its packing density, polarity, and the difference between the optical wavelength used and its maximum absorption wavelength [22-23]. Higher packing density or polarizability usually results in an increase in refractive index. Three common ways to fine-tune the refractive index are structure modification, physical aging, and guest doping of polymers.

Polarizability can be categorized into electronic, atomic, and dipole orientation types [24]. Electronic polarization arises from the slight skewing of the equilibrium electron distribution relative to the positive nuclei to which the distribution is associated. This process can be very fast ($\sim 10^{-15}$ s), as it solely require electrons movement. Atomic polarization necessitates a rearrangement of the nuclei in response to an electric field. The movement of heavy nuclei due to the applied field cannot follow the high oscillation of high frequency electric fields, and so the process is not as fast as the electronic type. Dipole polarization is caused by charge redistribution when a group of atoms with a net permanent dipole moment orients in space with respect to the applied electric field. Due to the requirement of large group masses reorientation, the process has time constants not lower than $\sim 10^{-9}$ s. Electronic polarization is the only type of polarization that occurs at optical frequencies [24].

Generally, the refractive index is higher in aromatic polymers compared to aliphatic polymers because of better packing and electronic polarizability. Moreover, highly π-conjugated dyes in polymers can raise the refractive index. As the temperature increases, the densification of atomic polymers leads to an increase in free volume and hence a higher refractive index.

Birefringence

Polymers, as opposed to inorganic crystals or glasses, can be molecularly engineered to achieve low birefringence. Aromatic moietiers tend to align with their planes oriented along the film surface [25-26]. In some polymers, birefringence can be as low as 10^{-5} to 10^{-6} [27] or as high as 0.24 (for aromatic polymers such as polyimides).

Temperature Dependence

The rapid change of the refractive index with temperature is one of the distinct characteristics of polymeric materials, which leads to large thermo-optic (T-O) effects. The rate of decrease is $10^{-4}/°\mathrm{C}$ (an order of magnitude larger than that of organic glasses). Since the thermal conductivity of polymers is low, strong T-O switches with low power consumption can be built. When combined with inorganic glass (with a positive T-O coefficient),the negative T-O coefficient of polymers enables them to achieve temperature independent waveguides [24].

Humidity Dependence

The humidity-induced change of the refractive index can affect the single mode waveguide performance if the core and cladding have different changes in their refractive indices. Even if the refractive indices of the core and cladding are similar, humidity will change the effective index of the waveguide, and therefore influence the performance of devices such as Bragg gratings and ultra wide band devices. Moisture absorption increases the refractive index of d-PMMA at room temperature, but decreases it at temperatures higher than 60°C [24].

Wavelength Dependence

The wavelength-dependent values for polymer are in the order of 10^{-6} nm^{-1} (comparable to those of SiO_2), which is much lower than those for semiconductors or doped glasses. This characteristic makes polymers more suitable for optical applications [24]. Moreover, basically, an optical system must be as free as possible from wavelength-dependent optical effects.

Environmental Stability

Yellowing is a phenomenon that occurs in polymer material when thermal aging progresses due to oxidation [20]. Partially conjugated molecular groups form and are characterized by broad ultraviolet absorption bands, which tail off in intensity through the visible region. The choice of linkage and monomers or oligomers determines the characteristics of the polymer, including surface energy, hardness, toughness, modules, water uptake, and stability against aging. Yellowing becomes almost negligible in fully halogenated materials because the absence of hydrogen precludes the formation of H-halogen products that result in carbon double bonds.

These unsaturated double bonds are the major reason for yellowing when they slowly oxidize over long-term thermal aging [24].

Polymers have a tendency to absorb water, which can deteriorate their properties. Those polymers composed of only hydrogen and carbon (i.e., polyethylene and polystyrene) are non-hydroscopic (highly water resistant), whereas polymers composed of oxygen or oxyhydrogen groups are hydroscopic [28].

2.3.3.4 Polymers in Optical Switching Devices

A well-known advantage of polymeric materials is their bandwidth. Intrinsic material bandwidths in the order of 350 GHz have been measured in organic materials due to their low and relatively frequency-independent dielectric constants and refractive indices.

By using a modified optical push-pull Mach-Zehnder Interferometer (MZI) architecture for the modulator design, a half-wave voltage of 0.8 V and a half-wave voltage-interaction length product of 2.2 Vcm can be achieved from a guest/host E-O PMMA by using a higher $\mu\beta$ polyene-type chromophore [29].

As push-pull architecture can reduce V_π by a factor of 2 compared with a single-arm modulation. The modulation efficiency of a device can be raised by 6 dB. A DC bias is necessary to keep the chromophores from orientational relaxation, which can lead to an r_{33} three times as high as that of the partially relaxed residual r_{33} after poling. Nevertheless, the applicability of such devices has been limited due to their polarization-dependent response.

CHAPTER 3
Determination of the Refractive Index Change Mechanisms

There are at least four mechanisms that can influence the refractive index of a doped material. Two of these mechanisms are electric field-related: linear E-O (Pockels Effect) and electro-refractive (E-R) effect. The other two are carrier-related and take place in a doped material: plasma effect and band filling effect. In the carrier-related effects, the change in refractive index is independent of the position inside the depletion region [15]. The total refractive index then can be determined as a superposition of these individual effects. This chapter presents a detailed description about these effects on the index of refraction of a semiconductor.

3.1 Electro-Optic Effect

3.1.1 Theory and Background

With respect to the E-O effect, a change in the refractive index is caused by the application of a DC or low frequency electric field. In an anisotropic material the refractive indices are modified by the external electric field and such modifications change the effect of the material on polarized light [30].

Since the optical wave travels a distance, which is orders in magnitude greater than its wavelength, even a minuscule change in the refractive index can cause considerable phase shifts. Moreover, since n varies only slightly with E, it can be expanded in a Taylors series as follows,

$$n(E) = n + a_1E + \frac{1}{2}a_2E^2 + ... \tag{3.1}$$

where $n = n(0)$, $a_1 = \frac{dn}{dE}|_{(E=0)}$ and $a_2 = \frac{d^2n}{dE^2}|_{(E=0)}$. The E-O coefficients are defined as: $r = -2a_1/n^3$ and $= -2a_2/n^3$. By substituting the electro optic coefficient,

$$n(E) = n - \frac{1}{2}rn^3E - \frac{1}{2}Rn^3E^2 + ... \tag{3.2}$$

in which the terms higher than the third are negligible. The values of r and R depend on the direction of the applied electric field as well as the light polarization.

The electro-optic effect can occur in the following two forms:

1. Linear (Pockels) effect: The refractive index change is proportional to the field.
2. Quadratic (Kerr) effect: The refractive index change is proportional to the square of the field.

3.1.1.1 Pockels Effect

When the third term in equation 3.2 is negligible compared to the second term, the refractive index can be expressed as follows:

$$n(E) = n - \frac{1}{2}rn^3E \tag{3.3}$$

where r is the Pockels (or linear E-O) coefficient. Typically, r values lie between 10^{-12} to 10^{-10} m/V, and therefore, the second term is in the order of 10^{-6} to 10^{-4}.

The crystals that are well-known to possess the Pockels effect are $NH_4H_2PO_4$ (ADP), KH_2PO_4 (KDP), $LiNbO_3$, $LiTaO_3$, and $CdTe$ [14].

3.1.1.2 Kerr Effect

The Kerr effect occurs in centrosymmetric materials such as gases, liquids, and certain crystals. Being invariant with the E reversal, n needs to be an even symmetric function as follows:

$$n(E) = n - \frac{1}{2}Rn^3E^2 + ... \tag{3.4}$$

where R is the Kerr (or quadratic E-O) coefficient. Typically, in crystals, R is 10^{-18} to 10^{-14} m^2/V^2 and in liquids 10^{-22} to 10^{-19} m^2/V^2 (resulting in a $\frac{1}{2}Rn^3E^2$ in the order of 10^{-6} to 10^{-2} for crystals and 10^{-10} to 10^{-7} for liquids).

3.1.1.3 Linear E-O Effect in Compound Semiconductors

The index of refraction of a crystal is related to its dielectric constant as $n = \sqrt{\epsilon_r}$ and hence [13],

$$\begin{bmatrix} \epsilon_{xx} & \epsilon_{xy} & \epsilon_{xz} \\ \epsilon_{yx} & \epsilon_{yy} & \epsilon_{yz} \\ \epsilon_{zx} & \epsilon_{zy} & \epsilon_{zz} \end{bmatrix} \begin{bmatrix} E_x \\ E_y \\ E_z \end{bmatrix} = \epsilon_0 \begin{bmatrix} n^2_{xx} & n^2_{xy} & n^2_{xz} \\ n^2_{yx} & n^2_{yy} & n^2_{yz} \\ n^2_{zx} & n^2_{zy} & n^2_{zz} \end{bmatrix} \begin{bmatrix} E_x \\ E_y \\ E_z \end{bmatrix} \tag{3.5}$$

The dielectric tensor must be symmetric to fulfill the energy conservation requirements. From the six remaining independent components, and by using $xx = 1$, $yy = 2$, $zz = 3$, $yz = 4$, $xz = 5$, and $xy = 6$, the linear electro-optic effect can be described as follows:

$$\begin{bmatrix} \Delta(\frac{1}{n^2})_1 \\ \Delta(\frac{1}{n^2})_2 \\ \Delta(\frac{1}{n^2})_3 \\ \Delta(\frac{1}{n^2})_4 \\ \Delta(\frac{1}{n^2})_5 \\ \Delta(\frac{1}{n^2})_6 \end{bmatrix} = \begin{bmatrix} r_{11} & r_{12} & r_{13} \\ r_{21} & r_{22} & r_{23} \\ r_{31} & r_{32} & r_{33} \\ r_{41} & r_{42} & r_{43} \\ r_{51} & r_{52} & r_{53} \\ r_{61} & r_{62} & r_{63} \end{bmatrix} \begin{bmatrix} E_x \\ E_y \\ E_z \end{bmatrix} \tag{3.6}$$

Crystal symmetry reduces the number of independent coefficients. In a crystal with a center of symmetry, e.g., Si, all r_{ijk} coefficients become zero. In other words, this kind of material does not have a linear E-O coefficient. In III-V semiconductors, however, the zinc-blend ($4\ \overline{3}$ m) crystal structure leads to a linear E-O tensor in the form as follows:

$$\begin{bmatrix} \Delta(\frac{1}{n^2})_1 \\ \Delta(\frac{1}{n^2})_2 \\ \Delta(\frac{1}{n^2})_3 \\ \Delta(\frac{1}{n^2})_4 \\ \Delta(\frac{1}{n^2})_5 \\ \Delta(\frac{1}{n^2})_6 \end{bmatrix} = \begin{bmatrix} 0 & 0 & 0 \\ 0 & 0 & 0 \\ 0 & 0 & 0 \\ r_{41} & 0 & 0 \\ 0 & r_{41} & 0 \\ 0 & 0 & r_{41} \end{bmatrix} \begin{bmatrix} E_x \\ E_y \\ E_z \end{bmatrix} \tag{3.7}$$

When an external electric field is applied, the index tensor becomes:

$$\begin{bmatrix} x & y & z \end{bmatrix} \begin{bmatrix} \frac{1}{n^2} & r_{41}E_z & r_{41}E_z \\ r_{41}E_z & \frac{1}{n^2} & r_{41}E_z \\ r_{41}E_z & r_{41}E_z & \frac{1}{n^2} \end{bmatrix} \begin{bmatrix} x \\ y \\ z \end{bmatrix} = 1 \tag{3.8}$$

For [001] crystal orientation and the z-directed modulating field ($E_x = E_y = 0$), the equation changes to:

$$\begin{bmatrix} x & y & z \end{bmatrix} \begin{bmatrix} \frac{1}{n^2} & r_{41}E_z & 0 \\ r_{41}E_z & \frac{1}{n^2} & 0 \\ 0 & 0 & \frac{1}{n^2} \end{bmatrix} \begin{bmatrix} x \\ y \\ z \end{bmatrix} = 1 \tag{3.9}$$

By rotating the $x-$ and $y-$axes 45° around the z-axis, the new $x'y'z'$ coordinate system becomes a diagonal tensor:

$$\begin{bmatrix} x' & y' & z' \end{bmatrix} \begin{bmatrix} \frac{1}{n^2} - r_{41}E_z & 0 & 0 \\ 0 & \frac{1}{n^2} + r_{41}E_z & 0 \\ 0 & 0 & \frac{1}{n^2} \end{bmatrix} \begin{bmatrix} x' \\ y' \\ z' \end{bmatrix} = 1 \tag{3.10}$$

As can be seen in Figure 3-1, for a z-axis along the 001 crystal plane, the $x'-$ and $y'-$axes are aligned with the 110 and 110 crystal axis. The refractive index increases along the x' and decreases in the y' direction.

$$\Delta n_{x'}(E) = +\frac{1}{2} r_{41} n^3 E_z \tag{3.11}$$

$$\Delta n_{y'}(E) = -\frac{1}{2} r_{41} n^3 E_z \tag{3.12}$$

$$\Delta n_{z'}(E) = 0 \tag{3.13}$$

Therefore, in this configuration, the TE mode is modulated, but the TM mode, whose main component lies in the 001 direction, is not modulated [13].

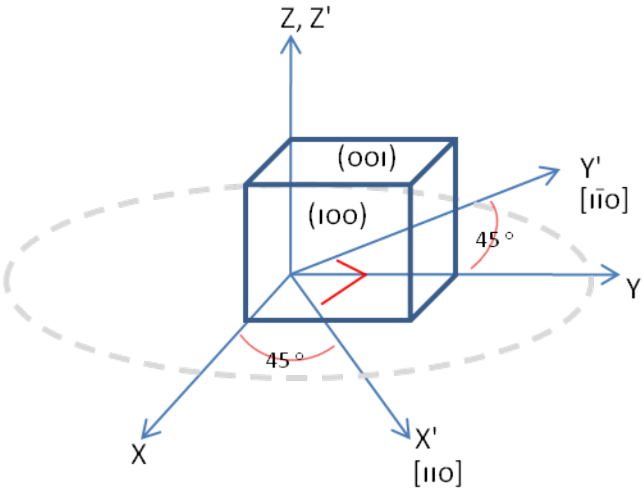

Figure 3–1: The crystal orientation relative to different coordinate systems used for the E-O effect calculation. For a field in the z-direction, TE_1, TE_2, and TM are along the x'-, y'-, and z-axes, respectively.

3.2 Determining the Required Parameters

Several models have been developed to compensate for the paucity of experimental values for different compositions at different wavelengths [31-34]. Although these models may predict divergence behaviour near the wavelengths corresponding to the bandgap energies, they also yield acceptable results at the rest of the wavelengths [13].

3.2.1 Dielectric Constant (Permittivity) Values

The frequency-dependent complex dielectric constant can be expressed as follows:

$$\varepsilon(\omega) = \varepsilon_1(\omega) + i\varepsilon_2(\omega) \tag{3.14}$$

where,

$$\varepsilon_1(\omega) = 1 + \frac{2}{\pi}\int_0^\infty \frac{\omega'\varepsilon_2(\omega')}{(\omega')^2 - \omega^2}d\omega' \tag{3.15}$$

$$\varepsilon_2(\omega) = 1 - \frac{2}{\pi}\int_0^\infty \frac{\varepsilon_1(\omega')}{(\omega')^2 - \omega^2}d\omega' \tag{3.16}$$

where $\varepsilon_1(\omega)$ is the frequency dependent dielectric constant, which can be determined as follows:

$$\varepsilon_1(\omega) = A_0\{f(\chi) + \frac{1}{2}[\frac{E_{g0}}{((E_{g0} + \Delta_{s0}))}]^{3/2} f(\chi_{s0})\} + B_0 \tag{3.17}$$

where,

$$A_0 = \frac{4}{3}(\frac{3\mu}{2})^{3/2}P^2 \tag{3.18}$$

$$f(\chi) = \chi^{-2}[2 - (1+\chi)^{1/2} - (1-\chi)^{1/2}] \tag{3.19}$$

$$\chi = \frac{\hbar\omega}{E_{g0}} \tag{3.20}$$

$$\chi_{s0} = \frac{\hbar\omega}{(E_{g0} + \Delta_{s0})} \tag{3.21}$$

and μ is the combined density of states mass, ω is the angular frequency, P is the momentum matrix element, E_0 is the lowest direct gap, Δ_{s0} is the spin-splitting gap, $\hbar\omega$ is photon energy, and B is the higher-lying gaps contribution[34].

In the following sections, the dielectric constant of different zinc-blende type semiconductors is calculated using the aforementioned numerical method.

3.2.1.1 Permittivity of Binary Material Systems

Binary compounds are the simplest III-V semiconductor systems. The A_0 and B_0 values used to calculate the permittivity of common binary compounds are listed in Table 3-1. By using these parameters, the calculated dielectric constant values of the binary alloys are summarized in Table 3-2.

Table 3–1: Parameters for ε_1 and r^s_{41} calculation

Compound	A_0	B_0	E_0 (10^{-12} m/V)	F_0 (10^{-12} m/V)
InP	8.4	6.6	-42.06	91.32
GaP	22.28	0.92	-83.31	16.6
$GaAs$	9.29	7.86	-71.48	123.16
$InAs$	4.36	10.52	-30.23	197.88

Table 3–2: The calculated values of dielectric constant, refractive index and E-O coefficient for binary alloys

Compound	ε_1	n	r_{41} (10^{-12} m/V)
InP	10.0124	3.1642	1.3402
GaP	9.9709	3.1577	1.0243
$GaAs$	11.36	3.3710	1.4990
$InAs$	14.6	3.6045	1.1414

3.2.1.2 Permittivity of Ternary and Quaternary Alloy Systems

The A_0 and B_0 necessary for calculating the dielectric constant of ternary and quaternary alloys can be interpolated from the quantities of their binary alloy components. In the following sections, the dielectric constant of $AlGaAs$ and $InGaAsP$ alloys is determined using this approach.

Permittivity of $AlGaAs$

The calculated permittivity of $AlGaAs$ for different Al fractions can be seen in Figure 3-2. The ternary parameters of $Al_xGa_{1-x}As$ can be calculated as a linear combination of the parameters of its ingredients, i.e., $GaAs$ and $AlAs$. Since the atomic weight of $AlAs$ is very close to that of GaP (101.9 vs. 100.7), and since atomic weight is proportional to the number of valence electrons, the values of GaP and $AlAs$ can be used interchangeably [35]. Thus, the ternary parameters can be determined as follows:

$$T_{AlGaAs}(x) = x.B_{GaP} + (1-x).B_{GaAs} \tag{3.22}$$

where T and B are the ternary and binary values, respectively, which can be substituted with A_0, B_0, E_0, and F_0. E_{g0} and Δ_{s0} for $Al_xGa_{1-x}As$ were calculated according to [33],

$$E_{g0}(x) = 1.424 + 1.266x + 0.26x^2 \tag{3.23}$$

$$\Delta_{s0}(x) = 0.34 - 0.5x \tag{3.24}$$

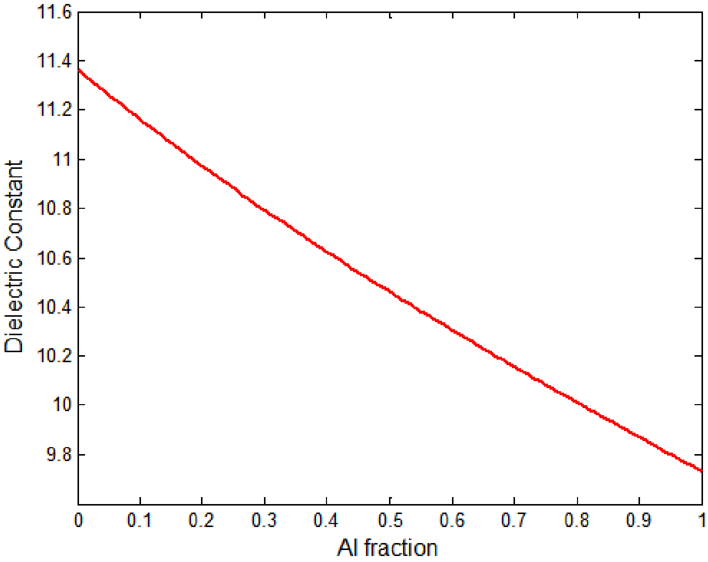

Figure 3–2: The calculated dielectric constant values of $AlGaAs$ as a function of the Al fraction (wavelength: 1550 nm, Temperature: 300k).

Permittivity of $InGaAsP$

Using the same approach as for the ternary alloys, the quaternary values of $In_{1-x}Ga_xAs_yP_{1-y}$ can be calculated as follows[13]:

$$Q_{InGaAsP}(x,y) = (1-x)(1-y)B_{InP} + x(1-y)B_{GaP} + xy.B_{GaAs} + (1-x)yB_{InAs} \tag{3.25}$$

where Q and B are the quaternary and binary values, respectively, which can be substituted with A_0, B_0, E_0, and F_0. E_{g0} and Δ_{s0} are calculated as follows [13]:

$$E_{g0}(y) = 1.35 - 0.72y + 0.12y^2 \tag{3.26}$$

$$\Delta_{s0}(y) = 0.12 + 0.3y + 0.11y^2 \tag{3.27}$$

The calculated dielectric constant values, as a function of y and x, are depicted in Figure 3-3. The results are calculated for a materials lattice matched to InP with a $x - y$ relationship as follows [13]:

$$x = \frac{0.1894y}{(0.4184 - 0.013y)} \tag{3.28}$$

In the designs used in this thesis, the $InGaAsP$ layers are adjacent to the InP layers (or substrate), and hence this model is plausible.

3.2.1.3 Effect of Doping on Permittivity

By solving the Poisson's equation and taking into account the carrier conservation, the effective sample permittivity can be expressed as,

$$\varepsilon^* = \varepsilon\left(\frac{1 + i\omega\tau}{i\omega\tau + \frac{tanhY}{Y}}\right) \tag{3.29}$$

with,

$$Y = \delta(1 + i\omega\tau)^{1/2} \tag{3.30}$$

and,

$$\delta = qd(\frac{n_0}{\varepsilon kT})^{1/2} \tag{3.31}$$

where τ is the dielectric relaxation time, d is the thickness, q is the electron charge, and k is the Boltzmann constant. As can be observed, the effect of doping on permittivity is insignificant, and is ignored throughout this work.

3.2.2 Refractive Index Values

Since ε_2 in equation 3.14 can be assumed to be zero near and below the lowest direct gap, the refractive index of the materials can be estimated as [33],

$$n(\omega) \approx [\varepsilon_1(\omega)]^{1/2} \tag{3.32}$$

3.2.2.1 Binary Material Systems

The calculated values of the refractive index for binary alloys can be found in Table 3-2.

3.2.2.2 Ternary and Quaternary Alloy Systems

In Figures 3-5 and 3-6, the refractive indices of ternary and quaternary alloys are depicted by using the same interpolation approach.

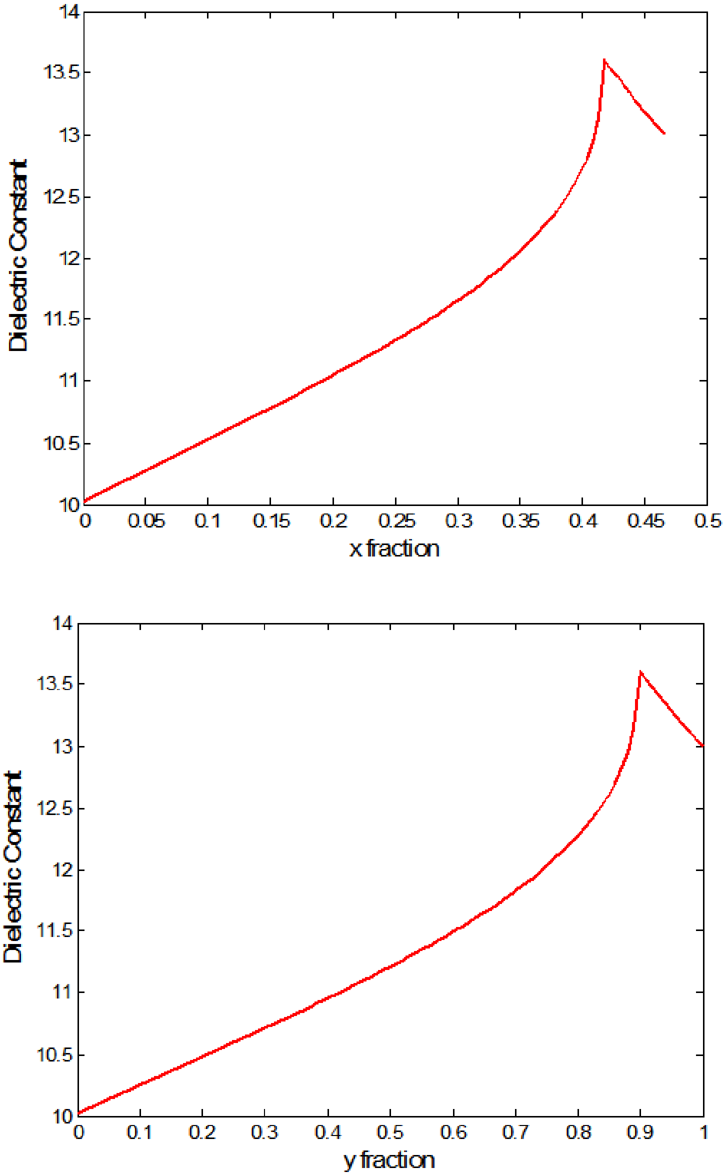

Figure 3–3: The calculated dielectric constant values of $In_{1-x}Ga_xAs_yP_{1-y}$ grown on an InP layer as a function of a) fraction x and b) fraction y (wavelength: 1550 nm, Temperature: 300k).

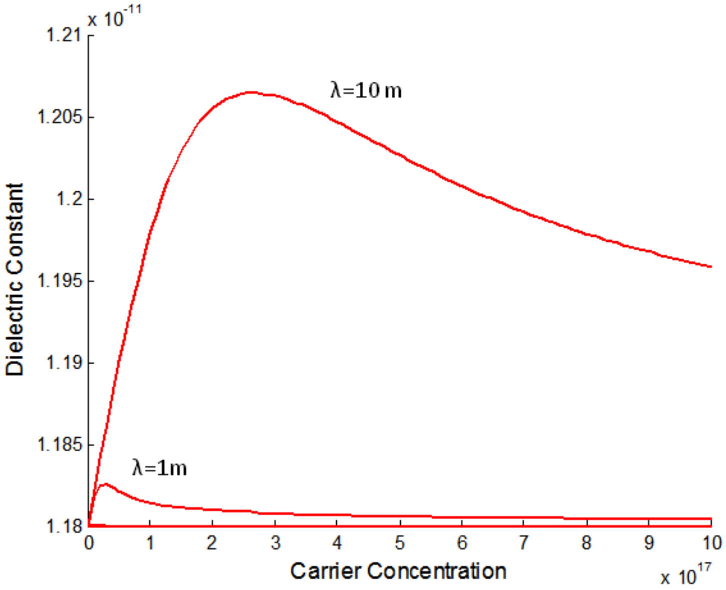

Figure 3–4: Effect of doping level on permittivity at wavelengths between 10^{-6} to 10 m. Thicknesses is 1 μm.

3.2.3 Electro-Optic Coefficient

The E-O effect in III-V compounds semiconductors is accompanied by piezoelectric and photoelastic phenomena. The applied electric field can cause a strain, i.e., elastic deformation in the material (the piezoelectric effect), which can induce an index change through the photoelastic effect. Therefore, r_{41} has the following two components:

$$r_{41} = r_{41}^{s} + r_{41}^{p} \tag{3.33}$$

The r_{41}^{p} contribution, which is caused by the photoelastic effect, is only considerable at low frequencies. On the other hand, r_{41}^{s} is observable at high frequencies well above the acoustic resonance of the material. The r_{41}^{s}, which is solely caused by the E-O

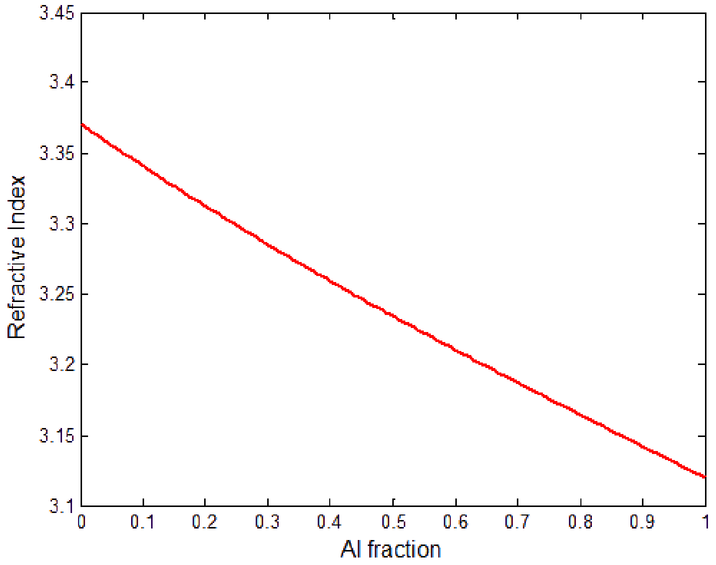

Figure 3–5: The calculated refractive index values of $AlGaAs$ as a function of Al fraction (wavelength: 1550 nm, Temperature: 300k)

effect, is also known as the clamped E-O coefficient [13]. The frequency-dependant r_{41}^{s} can be calculated as follows:

$$r_{41}^{s}(\omega) = |\frac{1}{\varepsilon_1^2(\omega)}[E_0 g(\chi) + F_0]| \tag{3.34}$$

$$E_0 = 1/2 A_0 E_{g0}^{-1} a \tag{3.35}$$

F_0 is the non-dispersive term that contains the higher-lying gaps contribution as well as the weak-dispersive Γ-point contributions [34]. E_0 and F_0 can be calculated based on the values in Table 3-1.

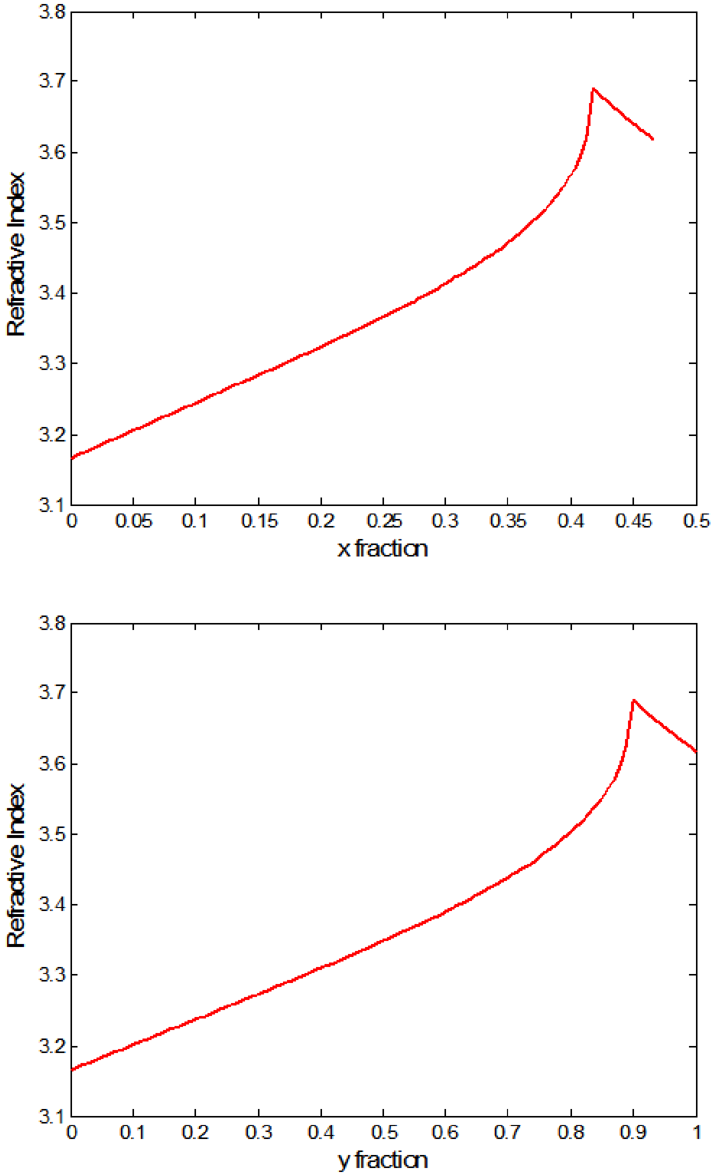

Figure 3–6: The calculated refractive index values of $In_{1-x}Ga_xAs_yP_{1-y}$ grown on an InP layer as a function of a) fraction x and b) fraction y (wavelength: 1550 nm, Temperature: 300k)

3.2.3.1 Binary Material Systems

The r_{41} values for the common binary alloys at the 1550 nm wavelength can be found in Table 3-2. In Figure 3-7 the r_{41} values calculated by the model are compared with the experimental data. As can be observed, the calculated values strongly agree with the experimental results.

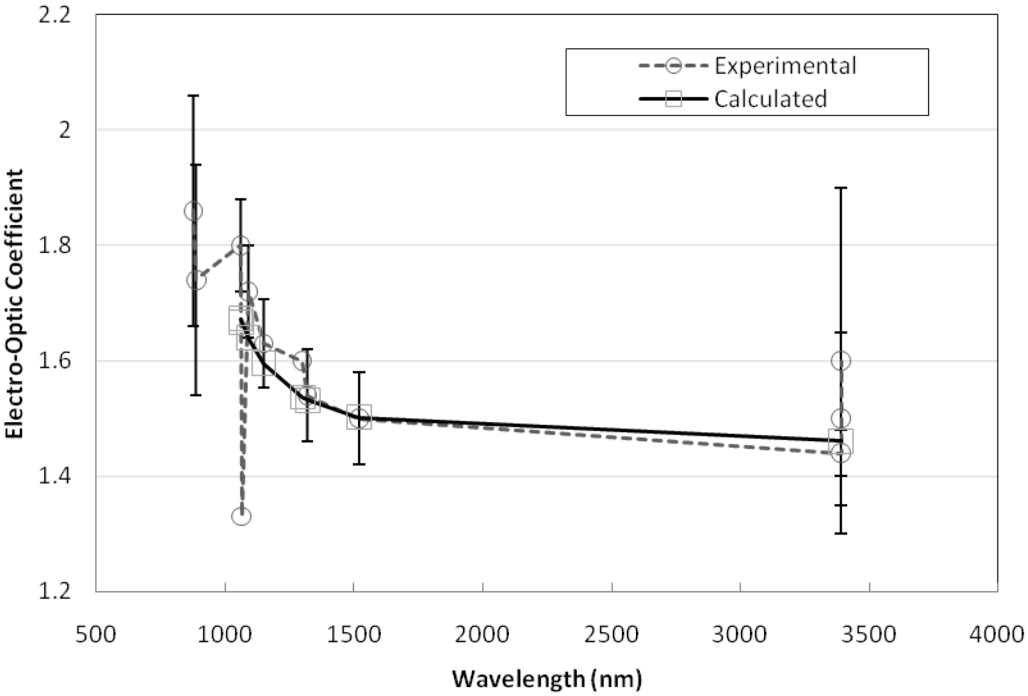

Figure 3–7: Linear E-O coefficients of *GaAs* at different wavelengths (calculated and experimental [taken from [13]]). The error bars belong to the experimental values.

3.2.3.2 Ternary and Quaternary Alloy Systems

In Figures 3-8 and 3-9, the E-O coefficients of the ternary and quaternary alloys are depicted by using the same interpolation approach.

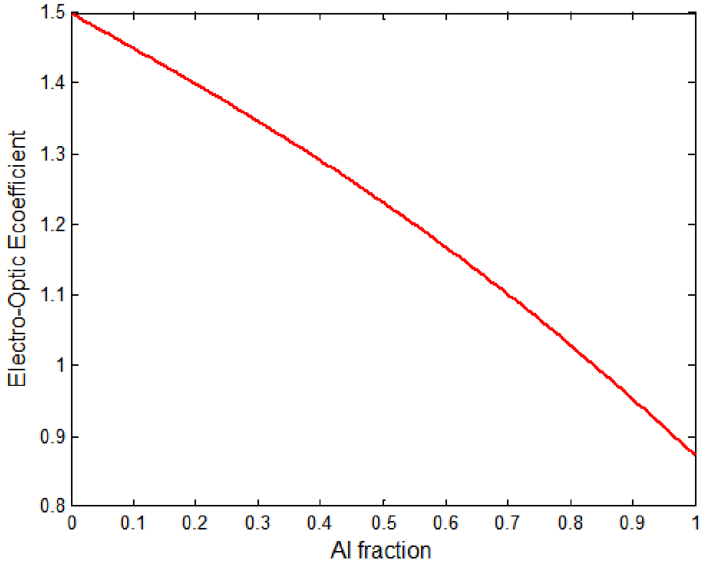

Figure 3–8: The calculated E-O coefficient values of $AlGaAs$ as a function of Al fraction (wavelength: 1550 nm, Temperature: 300k)

3.2.4 Effect of Doping On Materials Parameters

3.2.4.1 Bandgap Shrinkage

At high doping concentrations, the bandgap energy of semiconductors decreases. This effect is called bandgap narrowing. The amount of bandgap reduction increases with an increase in doping concentration. The wavefunctions of the electrons bound to the impurity atoms start to overlap as the density of the impurities increase. This overlap forces the energies to form an energy band rather than a discrete level.

$$\Delta E_g(N) = -\frac{q^2}{4\pi\varepsilon_s}(\frac{q^2 n}{\varepsilon_s kT})^{1/2} \tag{3.36}$$

where n is the doping density, and ε_s is the dielectric constant[36].

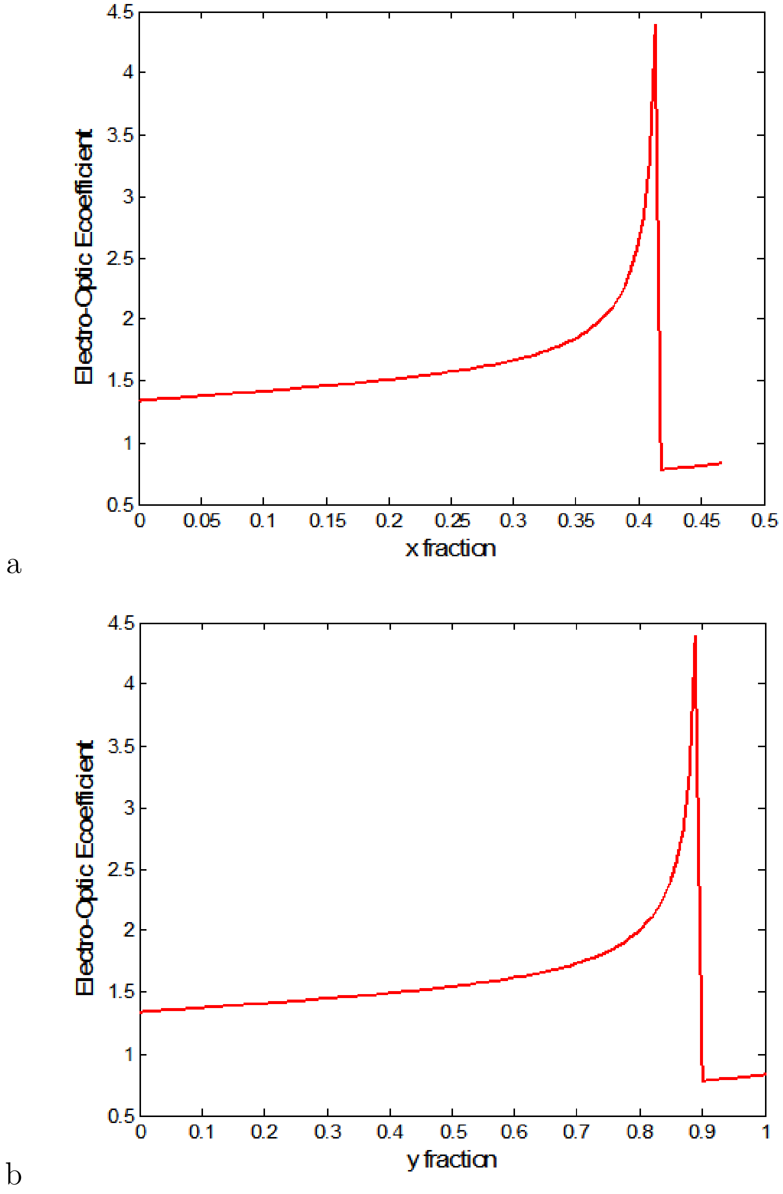

Figure 3–9: The calculated E-O coefficient values of $In_{1-x}Ga_xAs_yP_{1-y}$ grown on an InP layer as a function of a) fraction x and b) fraction y (wavelength: 1550 nm, Temperature: 300k)

3.2.4.2 Electric Field Distribution and Poisson's Equation

A p-n junction is the simplest form of p-type and n-type semiconductors in contact. A p-type semiconductor has a net density of acceptors, N_A, whereas an n-type semiconductor possesses a non-zero density of donors, N_D. Carrier diffusion plays the major role in the p-n diode operation. The electrostatic potential, φ(z) and potential energy of the electrons, i.e., $V(z) = e.\varphi(z)$ can be calculated using Poisson's equation[37] as follows:

$$\nabla^2 U + \frac{\partial}{\partial t}(\nabla . A) = -\frac{\rho}{\varepsilon_0} \tag{3.37}$$

on the n-side (-d_n<z<0):

$$\frac{d^2 V}{dz^2} = \frac{q^2}{2\varepsilon} N_D \tag{3.38}$$

and hence:

$$V(z) = V_n + \frac{q^2}{2\varepsilon} N_D (z + d_n)^2 \tag{3.39}$$

while on the p-side (0<z<d_p):

$$\frac{d^2 V}{dz^2} = -\frac{q^2}{2\varepsilon} N_A \tag{3.40}$$

which eventually yields:

$$V(z) = V_p - \frac{q^2}{2\varepsilon} N_D (z - d_p)^2 \tag{3.41}$$

and the electric field is simply calculated by differentiating the potential energy function. An analysis of the more intricate designs that comprise the epitaxial layers of semiconductors, requires a self-consistent calculation of Poisson's equation.

3.2.5 Electro-Refraction (E-R) Effect

The E-R or Kerr effect is a quadratic dependence of the refractive index on the Electric field and is found in all materials. Although the coefficients are usually very weak, according to the Franz-Keldysh relation, they can be enhanced in compound semiconductors at wavelengths near the bandgap energy [13]. The change in the refractive index can be estimated as [15],

$$\Delta n_{ER} = 3.45 \times 10^{-16} exp(\frac{3}{\lambda^3})E^2 \tag{3.42}$$

Where λ is the wavelength expressed in μm and E is the applied electric field in V/cm.

3.2.6 Plasma Effect

The plasma effect is the isotropic refractive index change due to the plasma frequency that arises from the free carrier absorption. The free carriers tend to decrease the refractive index with respect to that of the undoped material when the structure is reverse biased [15]. The resulting change in the refractive index can be formulated as,

$$\Delta n_{plasma} = -\frac{r_0 \lambda^2}{2\pi n}[\frac{N}{m_e} + \frac{P}{m_h}] \tag{3.43}$$

where $r_0 = 2.82 \times 10^{-13}$, N and P are the electron and hole densities, m_e is the electron mass, m_h is the hole effective mass, n is the refractive index and finally λ is the light wavelength. In $GaAs$, this change can be estimated as [13, 15],

$$\Delta n_{n-GaAs} = -9.6 \times 10^{-21} \frac{N}{nE^2} \tag{3.44}$$

$$\Delta n_{p-GaAs} = -1.8 \times 10^{-21} \frac{P}{nE^2} \tag{3.45}$$

where n is the refractive index and E is the photon energy. The plasma effect is generally smaller in a p-doped material [15].

The plasma effect is more pronounced in the depletion regions where carrier concentration change is significant [15]. The magnitude of the refractive index change is independent of the applied bias; however, the applied voltage determines the extent of the depletion region. The plasma frequency can also be modified by carrier injection. However, as already mentioned, this way of modifying the index is much slower since it takes longer to eliminate the injected carriers.

3.2.7 Band Filling Effect

The band filling effect occurs in a heavily doped material as a result of the displacement of Fermi level into or in proximity of the conduction or valence bands. The index change is more pronounced at photon energies near the bandgap. For doping levels below 5×10^{17} cm^{-3} there is a linear relationship between the refractive index change due to this effect and the carrier concentration [38],

$$\Delta n_{BF} \approx B(\lambda) N \tag{3.46}$$

At 1550nm wavelengths, the coefficient B is 2.4×10^{-21} and 1.2×10^{-21} cm^{-3} for n-$GaAs$ and p-$GaAs$, respectively [15]. Since the bandgap energy of $AlGaAs$ is larger than that of $GaAs$, the refractive index change in $AlGaAs$ is expected to be smaller. In a reverse biased device, the index change is negative due to band-emptying [39].

3.3 Summary

In this chapter the major mechanisms in refractive index modulation of a doped semiconductor were discussed. The overall change in the refractive index can be easily determined as a superimposition of changes due to the aforementioned effects. Figure 3-10 presents the typical diagram for changes in refractive index with carrier concentration, here in $GaAs$ and $Al_{0.06}Ga_{0.94}As$. The E-R effect can be neglected at the wavelength of interest, 1550nm.

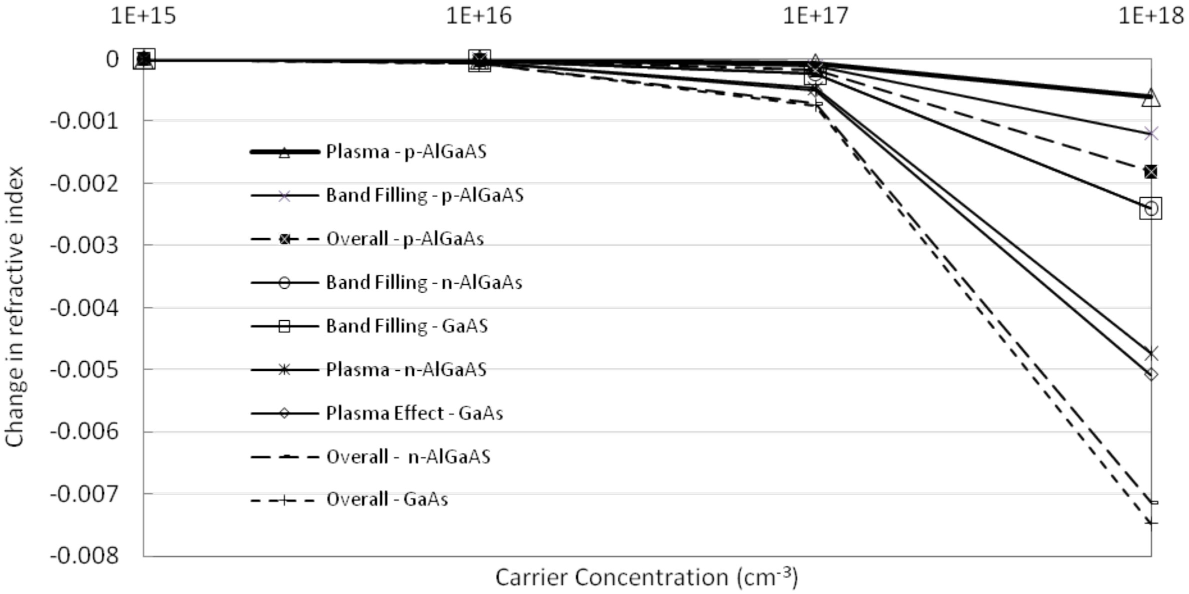

Figure 3–10: The calculated change in the refractive index with doping level for $GaAs$ and $Al_{0.06}Ga_{0.94}As$ at 1550nm wavelength.

CHAPTER 4
Device Design and Optimization

The first part of this chapter focuses on determination of the depletion region in which the mechanisms altering the index of refraction are operative. Afterwards, the length and voltage required for π-phase shift are determined and subsequently the final design of the Mach-Zehnder interferometric optical switch is presented. The effect of different doping profiles of the epitaxial layers as well as *Al* content of the cladding on the switch performance are also investigated.

4.1 Determination of Depletion Region

All the electric field- and carrier- related effects occur inside the depletion region whose thickness is contingent upon the nature of the junction, the doping levels and the applied reverse bias voltage [15]. The depletion region can be evaluated through solving the Poisson's equation for a p-n heterostructure.

When the core layer has a considerable amount of doping (N_d), the n side of the depletion region is limited to this layer (Figure 4-1 a) and the Poisson's equation is transformed to that of a simple p-n heterojunction [15] as follows,

$$x_n = \sqrt{\frac{2\varepsilon_1\varepsilon_2}{q}.\frac{N_A}{N_d}.\frac{(V_D - V_a)}{(\varepsilon_1 N_d + \varepsilon_2 N_A)}} \tag{4.1}$$

$$x_p = \sqrt{\frac{2\varepsilon_1\varepsilon_2}{q}.\frac{N_d}{N_A}.\frac{(V_D - V_a)}{(\varepsilon_1 N_d + \varepsilon_2 N_A)}} \tag{4.2}$$

where N_d and N_A are the doping of n-$GaAs$ (core) and p-$AlGaAs$ (upper cladding) layers, respectively, ε_1 and ε_2 are the permittivity of these layers, V_D is the built-in voltage at the heterojunction and V_a is the applied voltage (negative for a reverse bias).

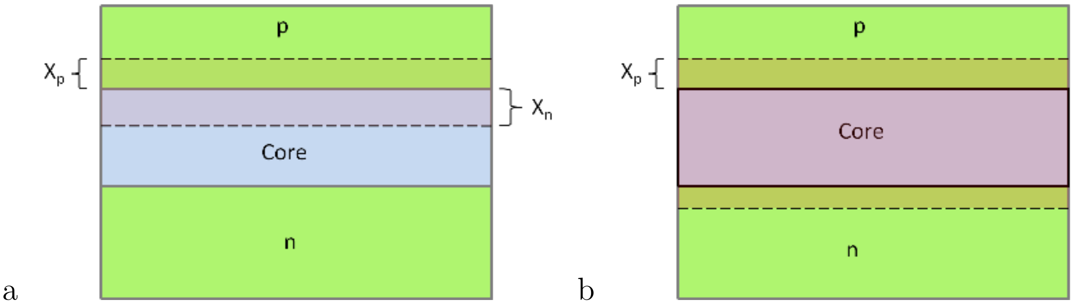

Figure 4–1: The Depletion region in the structure when a) the core with small doping level, b) core with high doping concentration.

When the doping level in the core region is small and/or the applied bias is large, the depletion region can be extended into the lower cladding (Figure 4-1 b). Therefore, the Poisson's equation has to be solved over the core, upper and lower claddings. The resulting value for the depletion regions is [15],

$$x_n - d = \frac{-qN_D d[\frac{N_d}{\varepsilon_2 N_A} + \frac{1}{\varepsilon_1}] + \sqrt{q^2 N_D d^2[\frac{N_D}{\varepsilon_1} - \frac{N_d}{\varepsilon_2}][\frac{N_d}{\varepsilon_2 N_A} + \frac{1}{\varepsilon_1}] + \frac{2qN_D}{\varepsilon_2}[1 + \frac{N_D}{N_A}][V_D - V_a]}}{\frac{qN_D}{\varepsilon_2}[1 + \frac{N_D}{N_A}]} \tag{4.3}$$

and the X_p region in the upper cladding equals to,

$$x_p = \frac{N_D(x_n - d) + N_d d}{N_A} \tag{4.4}$$

where N_D is the doping of the n-type lower cladding layer.

When the core has an insignificant amount of doping, the Kerr and Pockels effects are the only operative mechanisms. Nevertheless, there could also be plasma contributions from the doped claddings and/or if there is a depletion which takes place under the applied bias.

Figures 4-2 and 4-3 present the depletion region width X_n and X_p as a function of the bias voltage for different N_d concentrations at 10^{15} and 10^{18} cm^{-3} N_A contents. In a highly doped core ($N_d > 10^{16}$ cm^{-3}) the X_n depletion region is restricted to the core region, whereas in a moderately doped core ($N_d < 10^{16}$ cm^{-3}), the depletion region is extended beyond the core region. In the case of X_p depletion region, however, the depletion region increases as the doping level of the core is raised.

4.2 Determination of the L_π

After the individual refractive index changes are determined in the depletion regions, the change in the effective refractive index can be calculated. The phase change due to the change in the effective index is calculated as,

$$\Delta\varphi = 2\pi\Delta n_{eff}\frac{L}{\lambda} \tag{4.5}$$

where φ is the beam phase, n_{eff} is the effective refractive index, L is the waveguide length and λ is the wavelength. Moreover, the length for π-phase shift can be

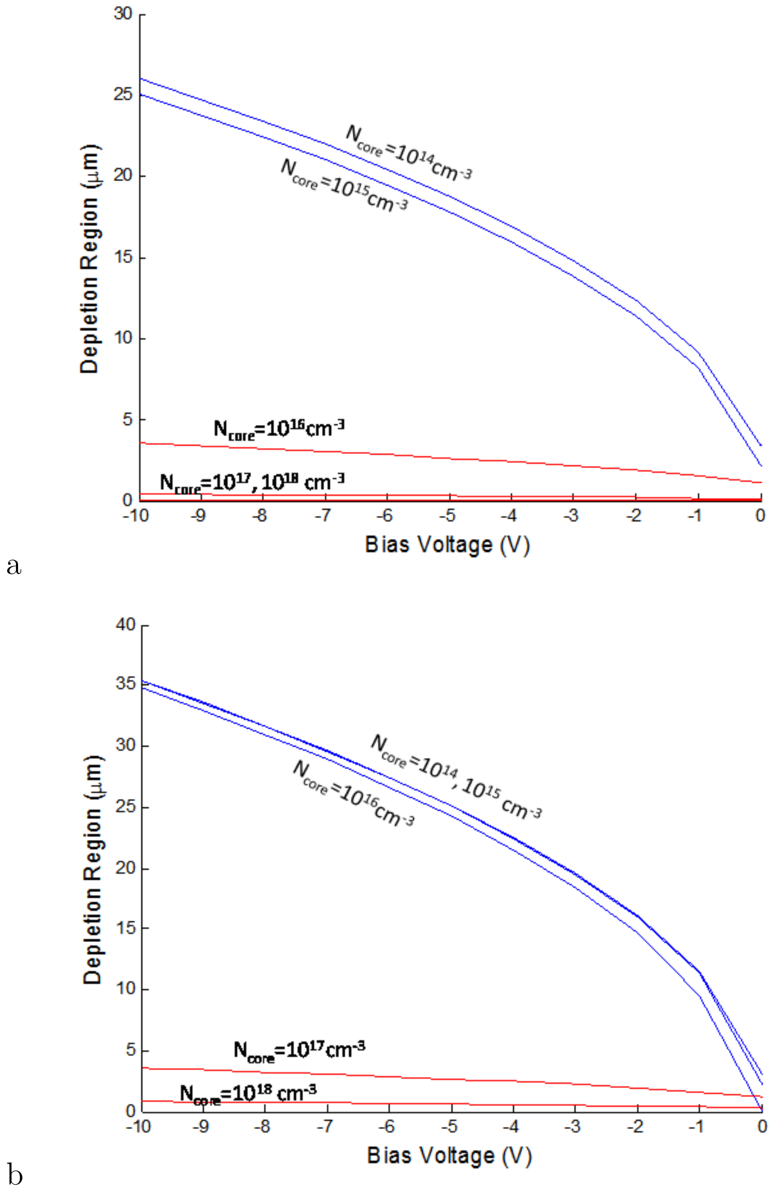

Figure 4–2: The effect of bias voltage on the depletion region width X_n for different N_d values in the following conditions: a) N_A=10^{15} and N_D=10^{15} cm^{-3} b) 10^{18} and 10^{15} cm^{-3} respectively c) 10^{15} and 10^{18} cm^{-3} respectively d) 10^{18} and 10^{18} cm^{-3} respectively.

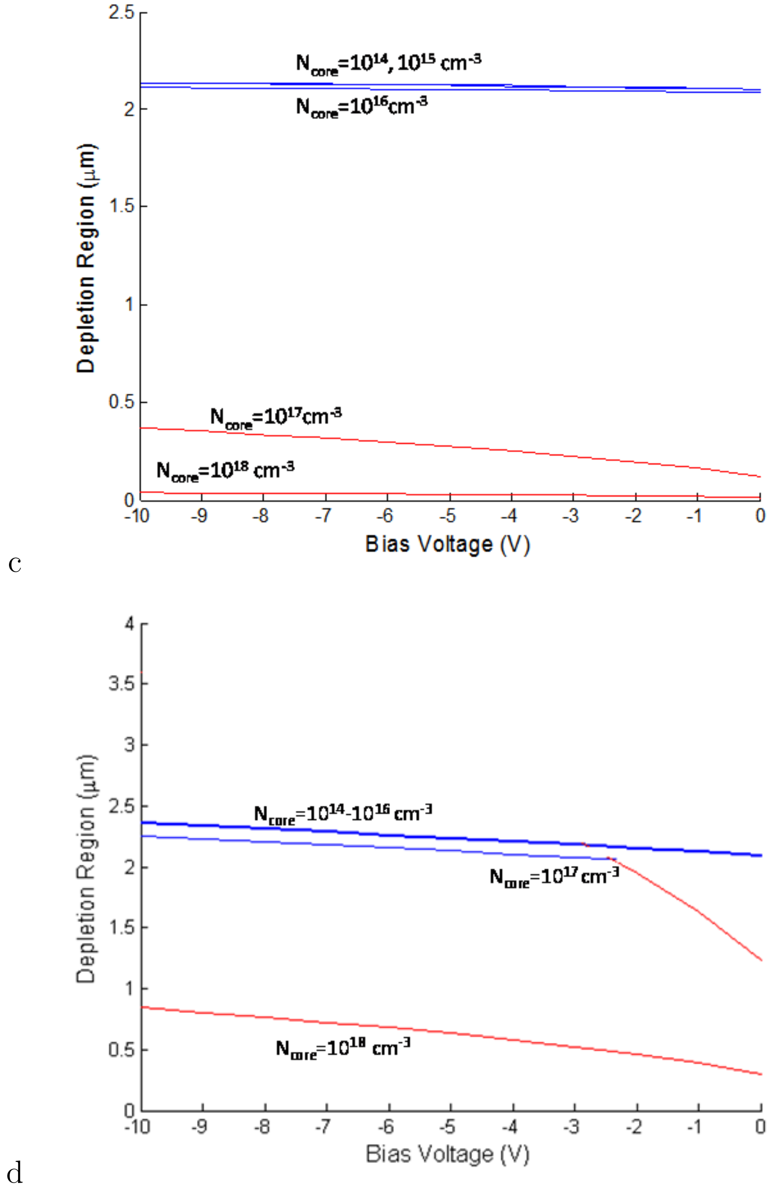

Figure 4–2 (continued)

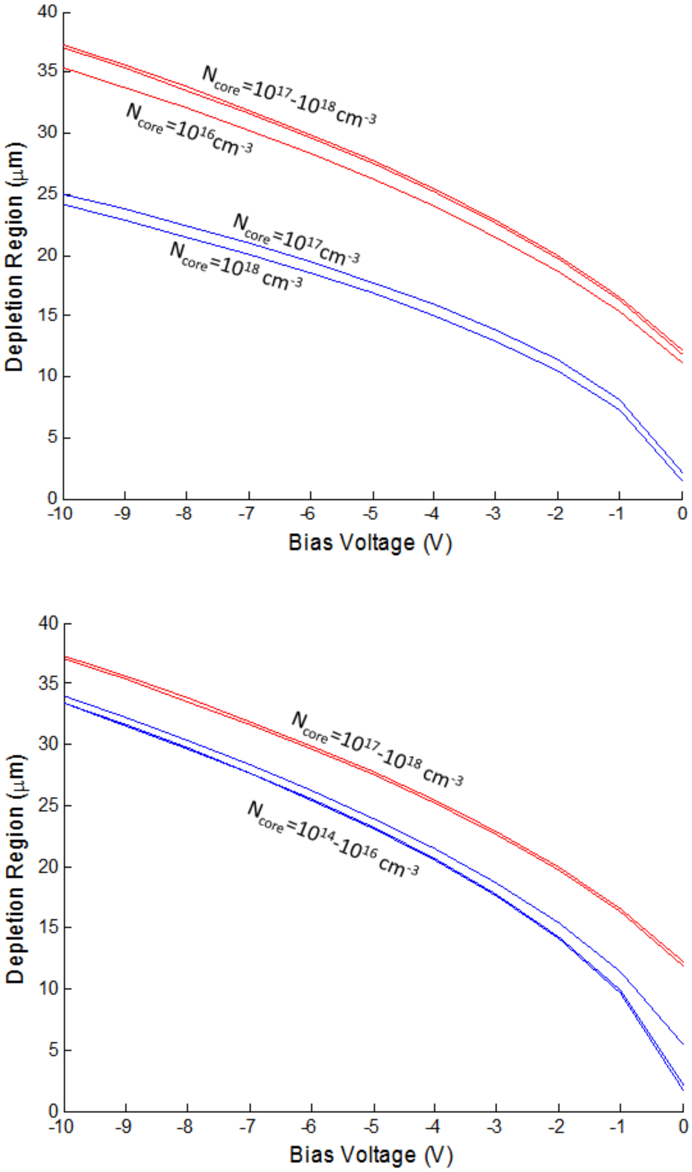

a

b

Figure 4–3: The effect of bias voltage on the depletion region width X_p for different N_d values in the following conditions: a) N_A=10^{15} and N_D=10^{15} cm^{-3} b) 10^{18} and 10^{15} cm^{-3} respectively c) 10^{15} and 10^{18} cm^{-3} respectively d) 10^{18} and 10^{18} cm^{-3} respectively.

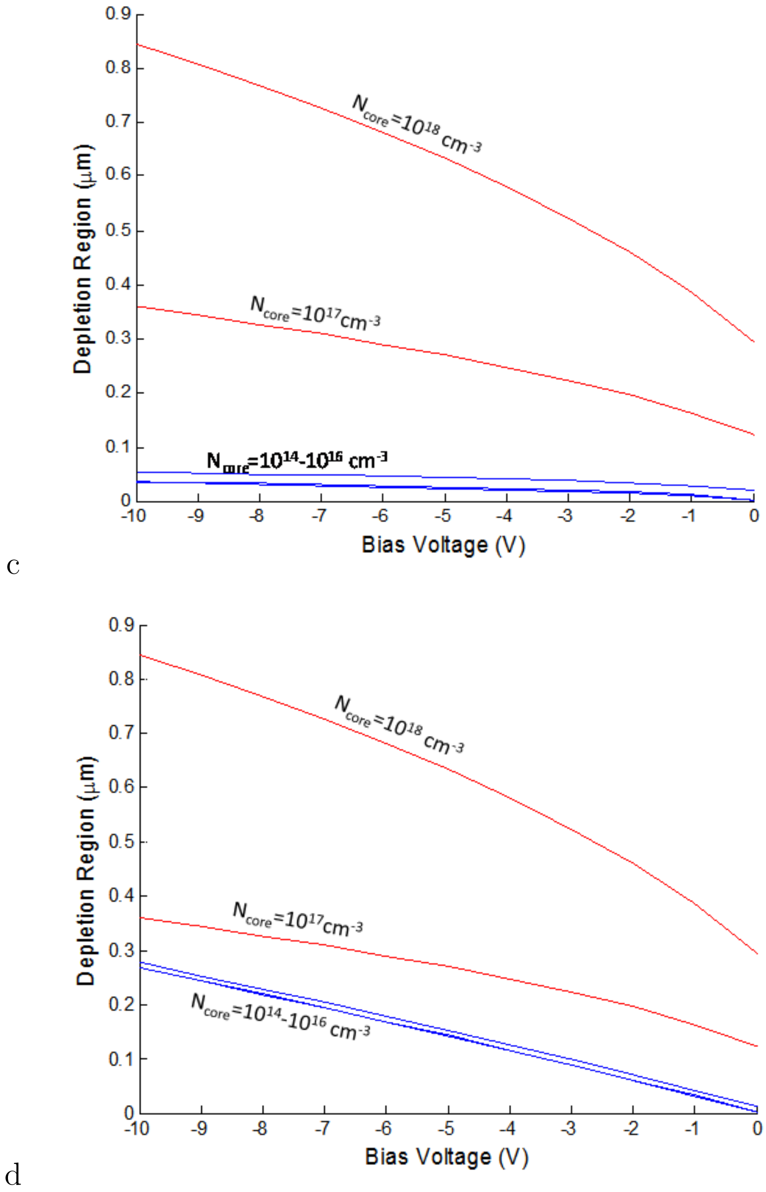

Figure 4–3 (continued)

determined as,

$$L_\pi = \frac{\lambda}{2\Delta n_{eff}} \tag{4.6}$$

In the present study, calculating the L_π was carried out using the OptiBPM 10.0 software. Figure 4-4 demonstrates a typical simulation result in which the beam phase before and after applying the 10V reverse voltage is illustrated at different beam traveling distances.

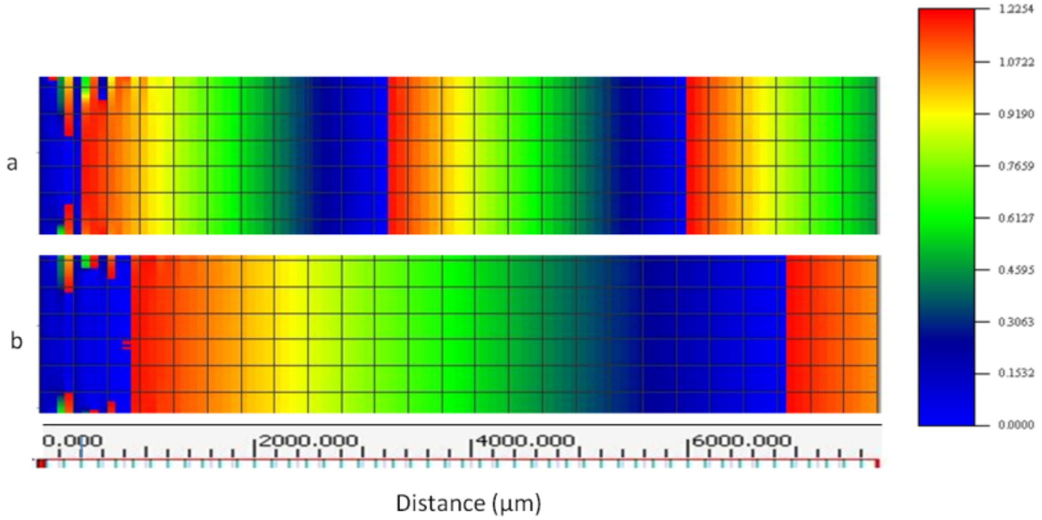

Figure 4–4: The beam phase a) before and b) after applying 10V reverse bias.

Figure 4-5 demonstrates the length required for π-phase shift due to a 10V reverse bias for different doping concentrations. The doping level of the lower cladding is assumed to be 10^{18} cm^{-3} in Figure 4-5a, and 10^{15} cm^{-3} in Figure 4-5b. It can be noticed that the L_π value is generally lower in lower claddings with 10^{18} cm^{-3} doping.

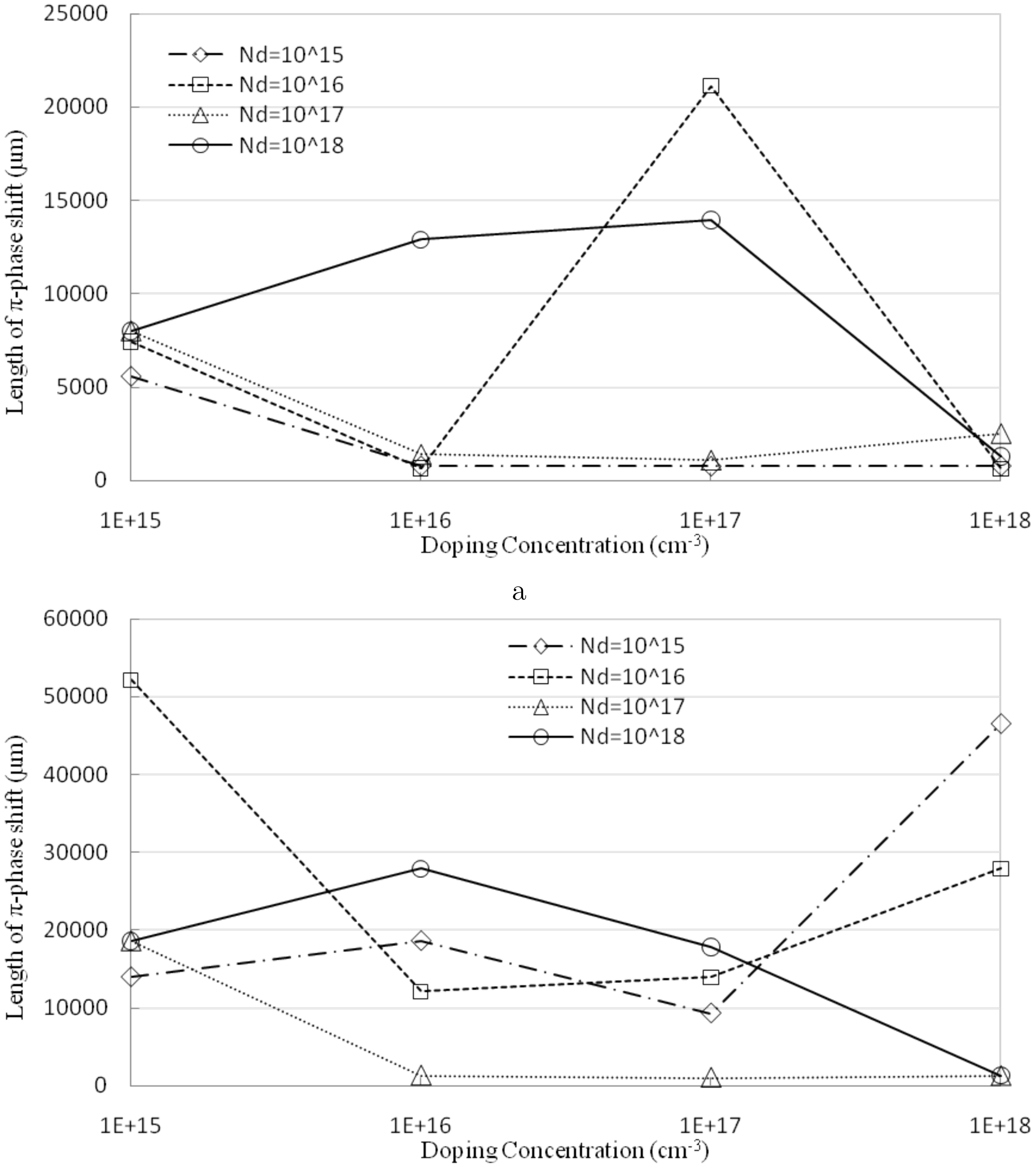

a

b

Figure 4–5: The calculated L_π as a function of the upper cladding doping for a) 10^{18} cm^{-3} and b) 10^{15} cm^{-3} lower cladding doping. (doping values are all in cm^{-3})

The corresponding switching voltage is determined as,

$$V_0 = \frac{\sqrt{3}\lambda d}{2n^3 r L_0} \tag{4.7}$$

where L_0 is the transfer distance, d is the coupling separation, n is the refractive index and r is the Pockels coefficient. Figure 4-6 depicts the V_π for different doping concentrations, also showing lower values in the case of lower claddings with 10^{18} cm^{-3} doping.

4.3 Design of Mach-Zehnder Optical Switch

In this work, the device is designed based on a double heterostructure (Figure 4-7). A double heterostructure, as opposed to a homojunction structure, allows separate optimization of the optical and electrical waveguide structure [4]. In this design, lateral confinement is obtained through localized etching [40]. The integrated switch is assumed to be produced on a z-cut *GaAs* wafer. Depending upon the material in use, the entire optical switch device is between 22 to 25 mm long and less than 40 μm wide. The width of the waveguide was chosen as 3 μm, which ensures the single mode operation.

As electrons or holes are released, charged donors or acceptors are left behind. These remnants scatter the carriers through coulomb interaction (ionized-impurity scattering). In order to avoid such problem, remote or modulation doping is used, which involves doping in one region and carriers migration in the other. This allows a large and uniform electric field to generate inside the i-region (undoped region) or over the core [13]. Nevertheless, according to Dagli [13], this design is not considered

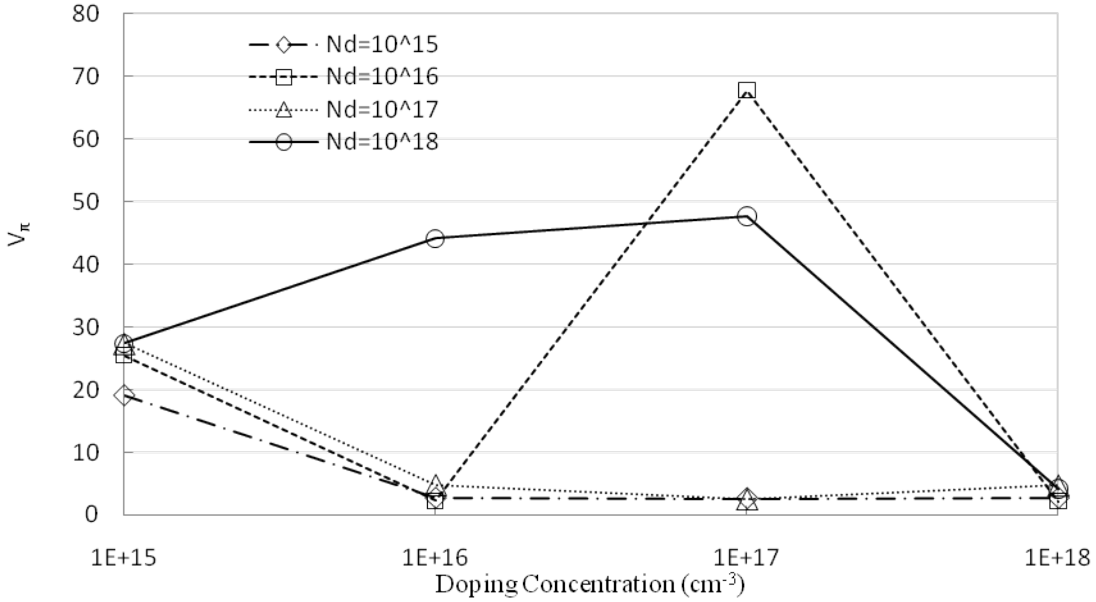

a

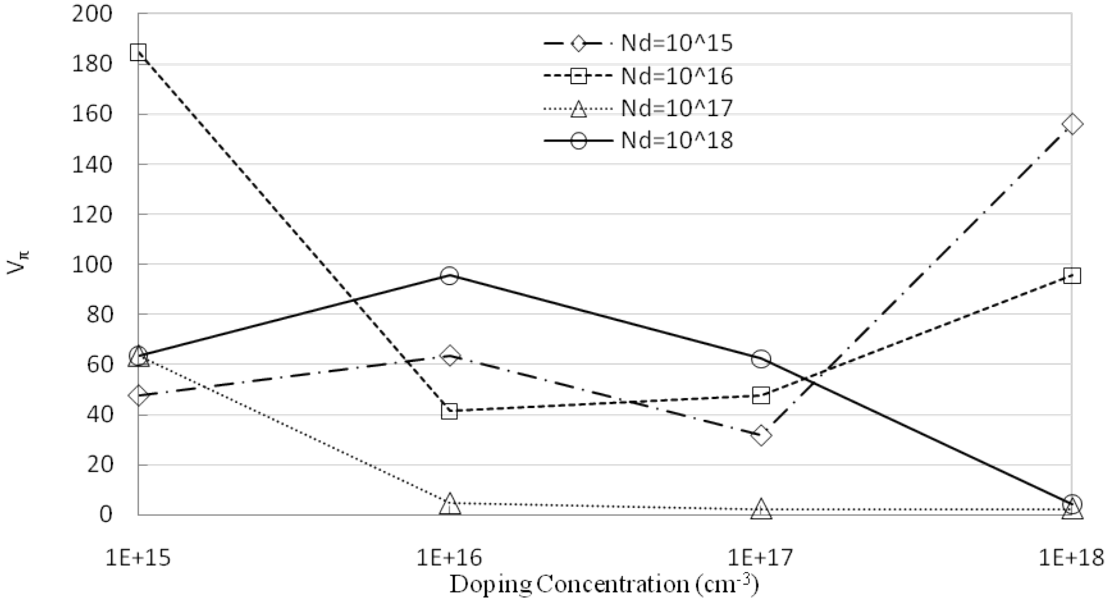

b

Figure 4–6: The calculated V_π as a function of the upper cladding doping for a) 10^{18} cm^{-3} and b) 10^{15} cm^{-3} lower cladding doping.(doping values are all in cm^{-3})

very useful for high-speed applications at microwave and millimetre wave frequencies. The reason is that the conductivity of even a heavily doped n-type semiconductor is not sufficient to keep Ohmic losses to minimum. This shortcoming seems to be less significant at optical wavelengths used in this study.

Figure 4-7b illustrates an alternative design with the p-metal and the etched rib supported by Benzocyclobutene (BCB). BCB is a polymer with a low dielectric constant (2.365444 according to [41]) that can serve as an insulating dielectric material in chips, interconnects, and other photonic devices [42]. In addition to a low dielectric constant, this material has a low dissipation factor, low moisture uptake and good thermal stability. Such properties make BCB a very good candidate for portable, high-frequency microelectronic systems [43].

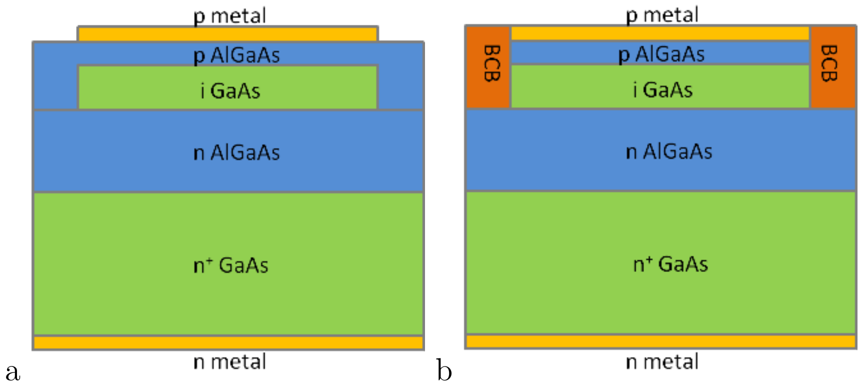

Figure 4–7: The double-heterostructure based on which the optical switch is designed.

The Mach-Zehnder optical switch was designed based on a $GaAs/AlGaAs$ double heterostructure. In this structure, the thickness and refractive index of each layer can be precisely adjusted, which facilitates the optimization of waveguide. The thickness of the substrate, upper cladding, core and lower cladding were selected based on the findings of Menard et al. [6]. According to Menrad et al., simultaneous optimization of the index contrast and layer thicknesses is necessary for minimizing losses. Using the 2-D eigenmode expansion algorithm, they calculated the radiation loss for different values of refractive index contrast and core thickness. For each case, the top cladding thickness was varied between 0.5 and 3.0 μm and only the most efficient configuration was considered. Finally, single mode operation was verified for each configuration. Based on these results, a double heterostructure with the core thickness of 2.1 μm, the top cladding of 0.6 μm and lower cladding of 5.5 μm was selected. The optimum index contrast found for this structure pertained to $AlGaAs$ claddings with an Al fraction of 0.06. The layers specifications and the switch layout can be observed in Figures 4-8 and 4-9, respectively.

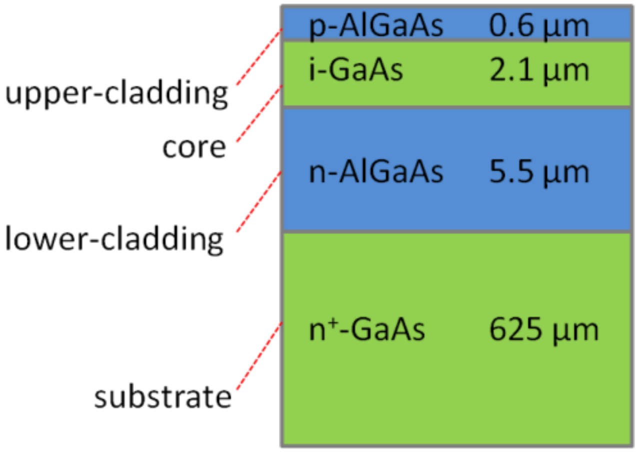

Figure 4–8: The epitaxial layers thickness and materials used for the design.

In this configuration, only TE modes are being excited and the optical mode is being supported by the vertical electric field in the structure. According to equation

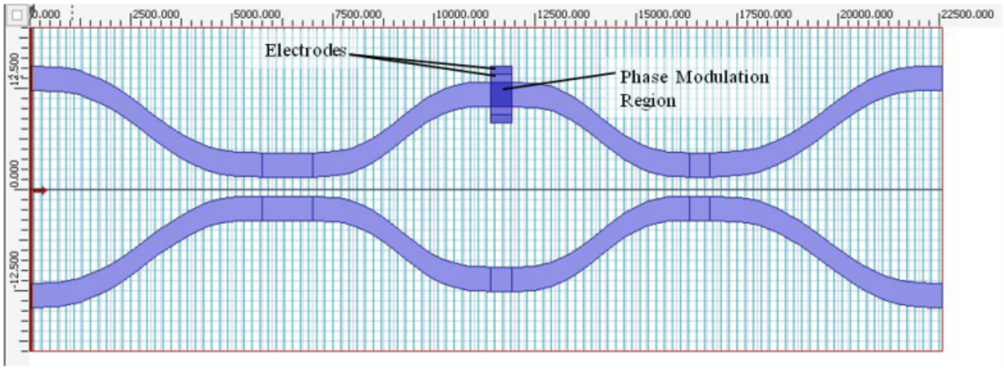

Figure 4–9: The layout of the 2×2 Mach-Zehnder interferometric optical switch (the scales are in μm).

3.10, the E-O tensor of $GaAs$ has non-zero components (r_{41}) in the crystal coordinate system. The E-O relationship can be rewritten as,

$$n' = n + \frac{n^3}{2}(r_H E_x + r_V E_V) \tag{4.8}$$

where r_H and r_V are the E-O coefficients in the horizontal and vertical directions. In this design, however, the waveguide axis is rotated by 45° around the crystal (z-) axis in a way that the vertical electric field affects the TE mode of the waveguide by an E-O coefficient of r_{41}. The horizontal component of electric field is not affected by the horizontally polarized TE mode and can be taken as zero (r_H=0).

4.3.1 Simulation Conditions

The beam propagation studies were performed using the OptiBPM 10.0 software. The simulation was 3D-Isotropic with 300 mesh points. The E-O effect was simulated within the software, whereas the carrier related effects and the depletion region widths were calculated according to the abovementioned sections and imported into the software. The substrate doping was chosen as 10^{18} cm^{-3} to ensure sufficient conductivity of the electric field.

4.3.2 Input Beam Characteristics

The input beam in the OptiBPM software was chosen as Gaussian whose intensity was non-uniform along the direction normal to the waveguide plane. By calculating the effective refractive index, the changes in the intensity were taken into account. The wavelength was taken as 1550 nm and the polarization as transverse-electric (TE) and the propagation step equal to 1.55.

4.3.3 Electrode Properties

The electrodes were assumed to be perfect conductors which do not intersect the guided mode. For the simulations, the refractive index of the electrode was selected slightly smaller than the upper cladding index. A buffer layer with a low dielectric constant was assumed between the electrodes and the substrate to reduce the losses due to the metallic cover of the waveguide [44].

4.4 Beam Propagation Study

The doping profiles that lead to the lowest L_π values were selected from the results shown in Figure 4-5. These profiles can lead to the most efficient phase modulation, and hence more compact switches. The designs based on these selected profiles are examined in the following sections.

4.4.1 $Al_{0.06}Ga_{0.94}As$-Based Claddings

4.4.1.1 $N_A18 - N_d15 - N_D18$ Doping Profile

In this profile, the upper cladding, core and lower cladding have the doping concentrations of 10^{18}, 10^{15} and 10^{18} cm^{-3}, respectively. The beam propagation, before and after applying 10V reverse bias can be seen in Figure 4-10.

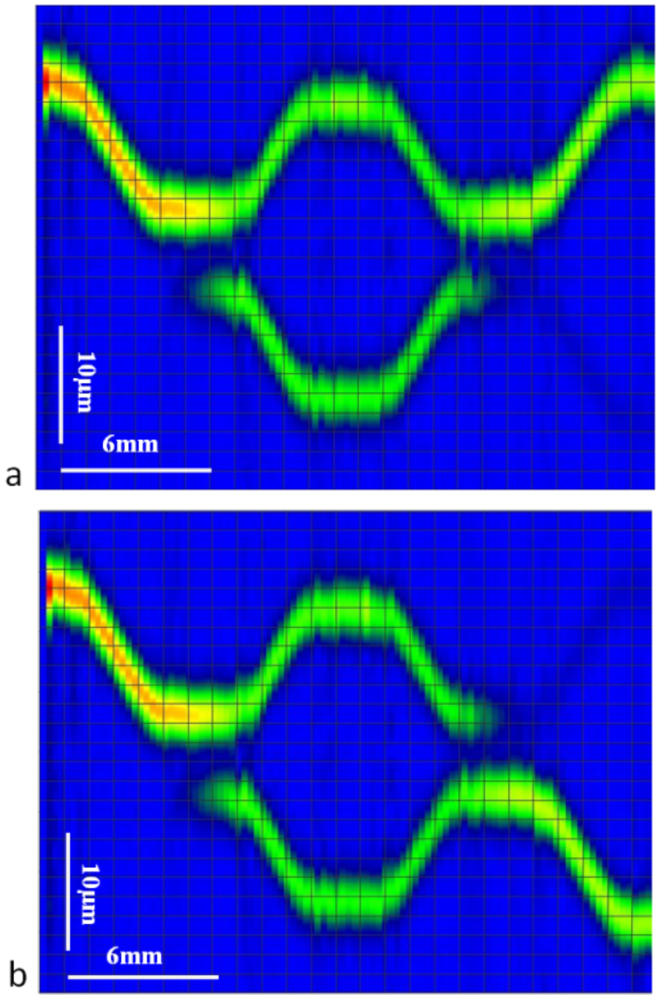

Figure 4–10: The beam propagation in the waveguide based on $N_A18 - N_d15 - N_D18$ doping profile a) before and b) after applying the 10V reverse-bias voltage.

4.4.1.2 $N_A16 - N_d15 - N_D18$ Doping Profile

In this profile, the upper cladding, core and lower cladding have the doping concentrations of 10^{16}, 10^{15} and 10^{18} cm^{-3}, respectively. The beam propagation, before and after applying 10V reverse bias is shown in Figure 4-11.

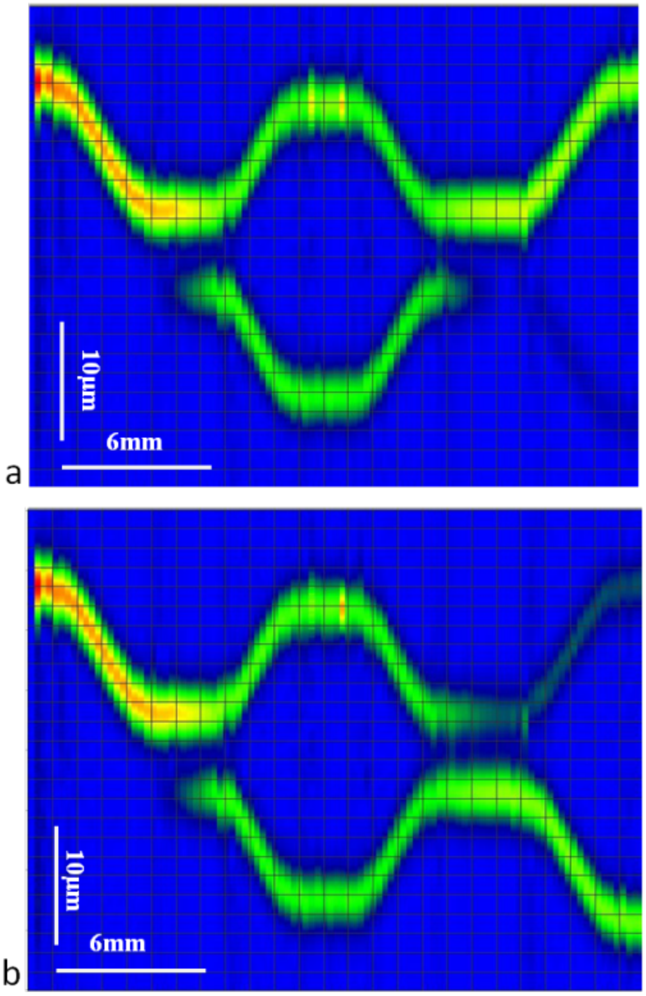

Figure 4–11: The beam propagation in the waveguide based on $N_A16 - N_d15 - N_D18$ doping profile a) before and b) after applying the 10V reverse-bias voltage.

4.4.1.3 $N_A17 - N_d17 - N_D18$ Doping Profile

In this profile, the upper cladding, core and lower cladding have the doping concentrations of 10^{17}, 10^{17} and 10^{18} cm^{-3}, respectively. Figure 4-12 shows the beam propagation, before and after applying 10V reverse bias.

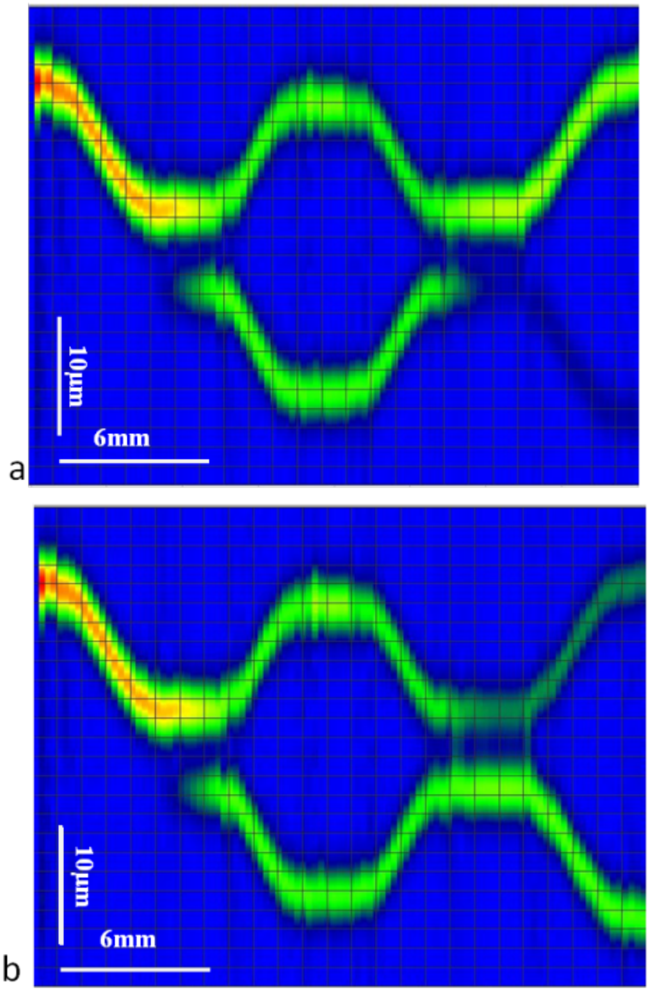

Figure 4–12: The beam propagation in the waveguide based on $N_A17 - N_d17 - N_D18$ doping profile a) before and b) after applying the 10V reverse-bias voltage.

4.4.1.4 $N_A17 - N_d17 - N_D15$ Doping Profile

In this profile, the upper cladding, core and lower cladding have the doping concentrations of 10^{17}, 10^{17} and 10^{15} cm^{-3}, respectively. The beam propagation, before and after applying 10V reverse bias can be seen in Figure 4-13.

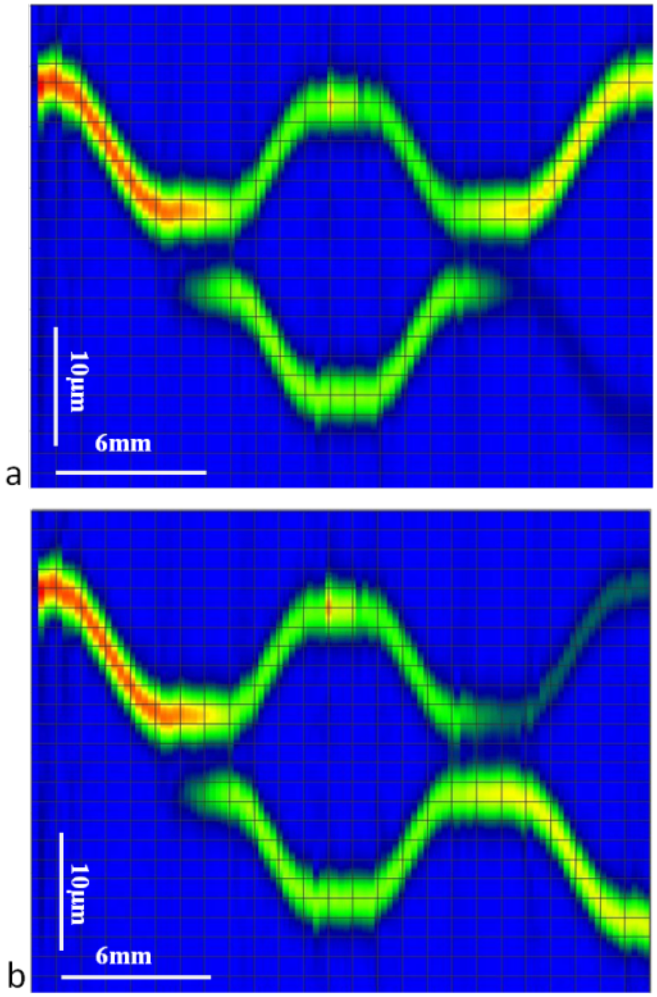

Figure 4–13: The beam propagation in the waveguide based on $N_A17 - N_d17 - N_D15$ doping profile a) before and b) after applying the 10V reverse-bias voltage.

4.4.1.5 $Al_{0.1}Ga_{0.9}As$-Based Cladding

The most efficient doping profile for an $Al_{0.1}Ga_{0.9}As$ was found to have 10^{18}, 10^{18} and 10^{18} cm^{-3} in the upper cladding, core and lower cladding layers, respectively. The beam propagation, before and after applying 10V reverse bias can be seen in Figure 4-14.

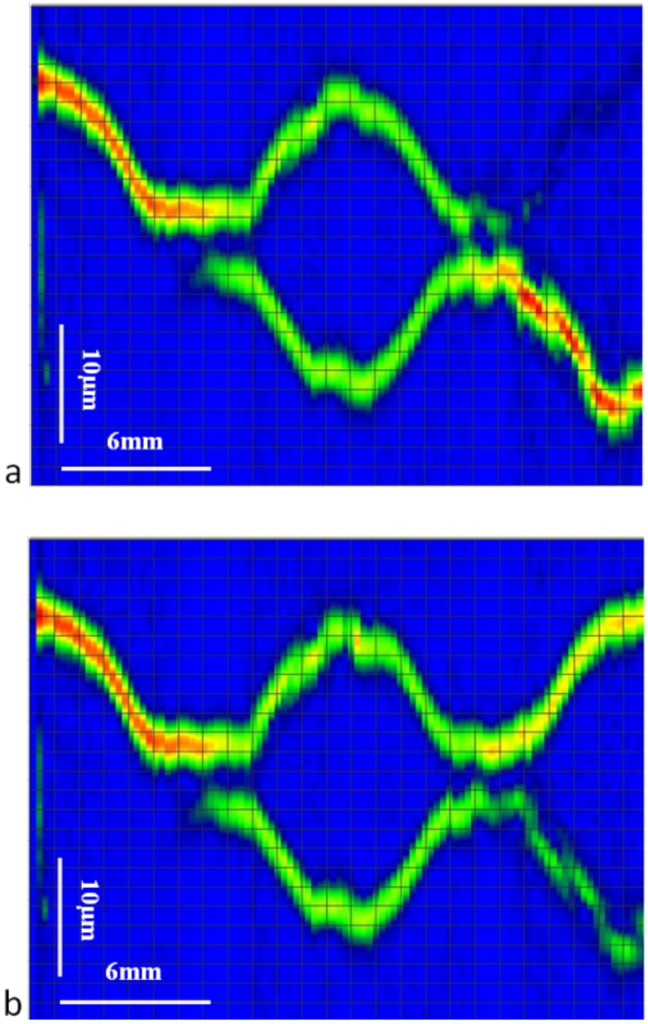

Figure 4–14: The beam propagation in the waveguide based on $Al_{0.1}Ga_{0.9}As$ claddings a) before and b) after applying the 10V reverse-bias voltage.

Moreover, in the case of $Al_{0.15}Ga_{0.85}As$ the most efficient doping profile was 10^{18}, 10^{16} and 10^{18} cm^{-3}; however, the switch suffers from a low extinction ratio as discussed later.

Table 4-1 summarizes the transfer distance and overall length of the abovementioned switch designs.

Table 4–1: The switch dimensions

X	Upper Clad N_A (cm^{-3})	Core N_d (cm^{-3})	Lower Clad N_D (cm^{-3})	Transfer Distance (μm)	Overall Length (μm)
0.06	10^{18}	10^{15}	10^{18}	1400	24240
0.06	10^{16}	10^{15}	10^{18}	1275	24920
0.06	10^{17}	10^{17}	10^{18}	1400	24950
0.06	10^{17}	10^{17}	10^{15}	1030	23840
0.10	10^{18}	10^{18}	10^{18}	1000	24040
0.15	10^{18}	10^{16}	10^{18}	515	22575

4.5 Power Considerations

Figure 4-15 represents the variations in the relative power in the z-direction. As can be seen, the losses are generally lower in the waveguides made of $Al_xGa_{1-x}As$ claddings with x values higher than 0.06. Since the refractive index of $Al_xGa_{1-x}As$ reduces by the x value, higher x values result in claddings with lower indices, and therefore more confinement in the core region.

Figure 4-16 demonstrates the change in the overlap power of the switch in the z-direction. The overlap power is lowest in the lower cladding with doping concentration of merely 10^{15} cm^{-3}.

The significant reduction in the electric power in a waveguide with 10^{15} cm^{-3} doped lower cladding can be explained by the conduction band energy variations

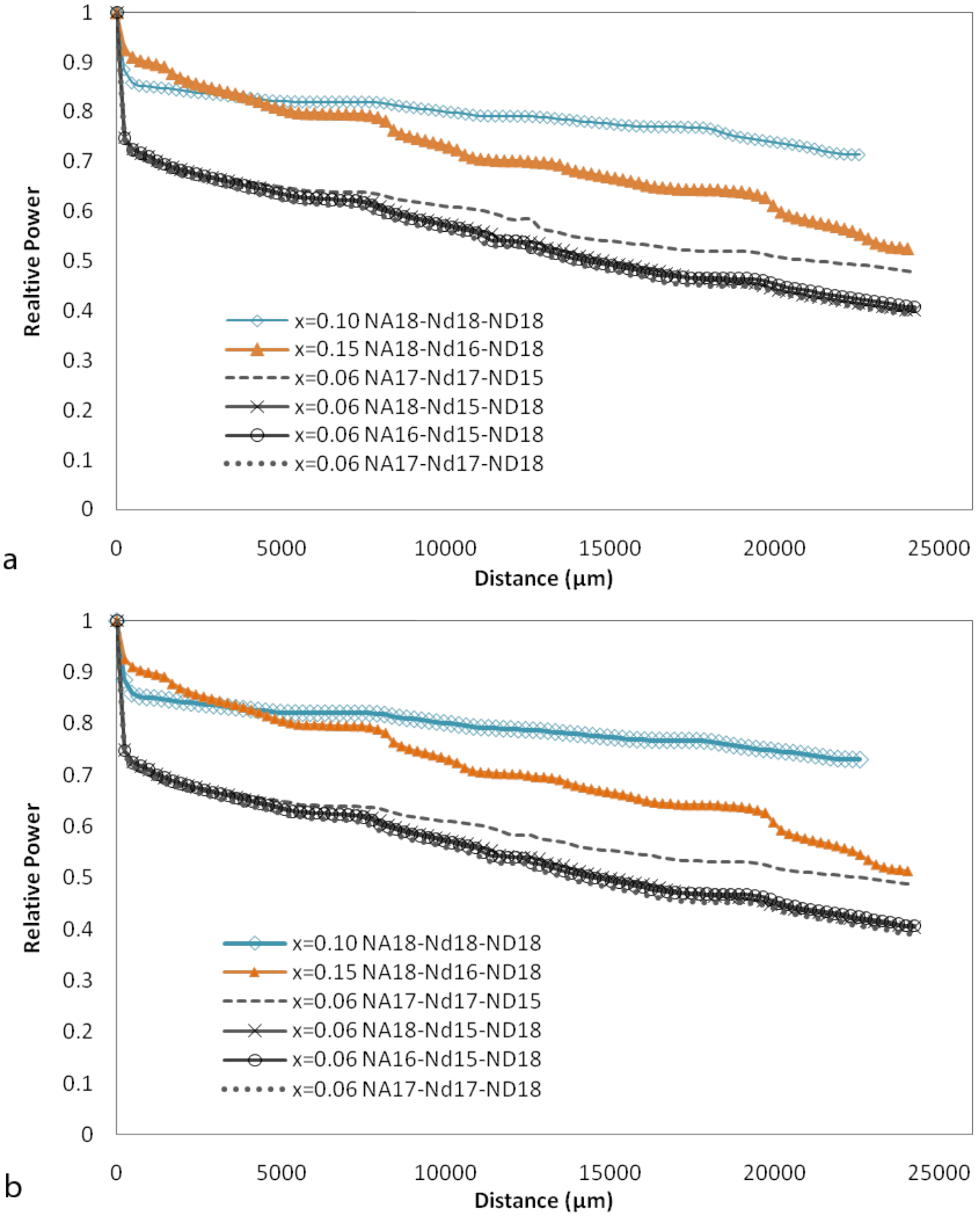

Figure 4–15: The relative power variations in the waveguides with different doping profiles a) before and b) after applying the 10V reverse-bias voltage. a) 0V b) 10V

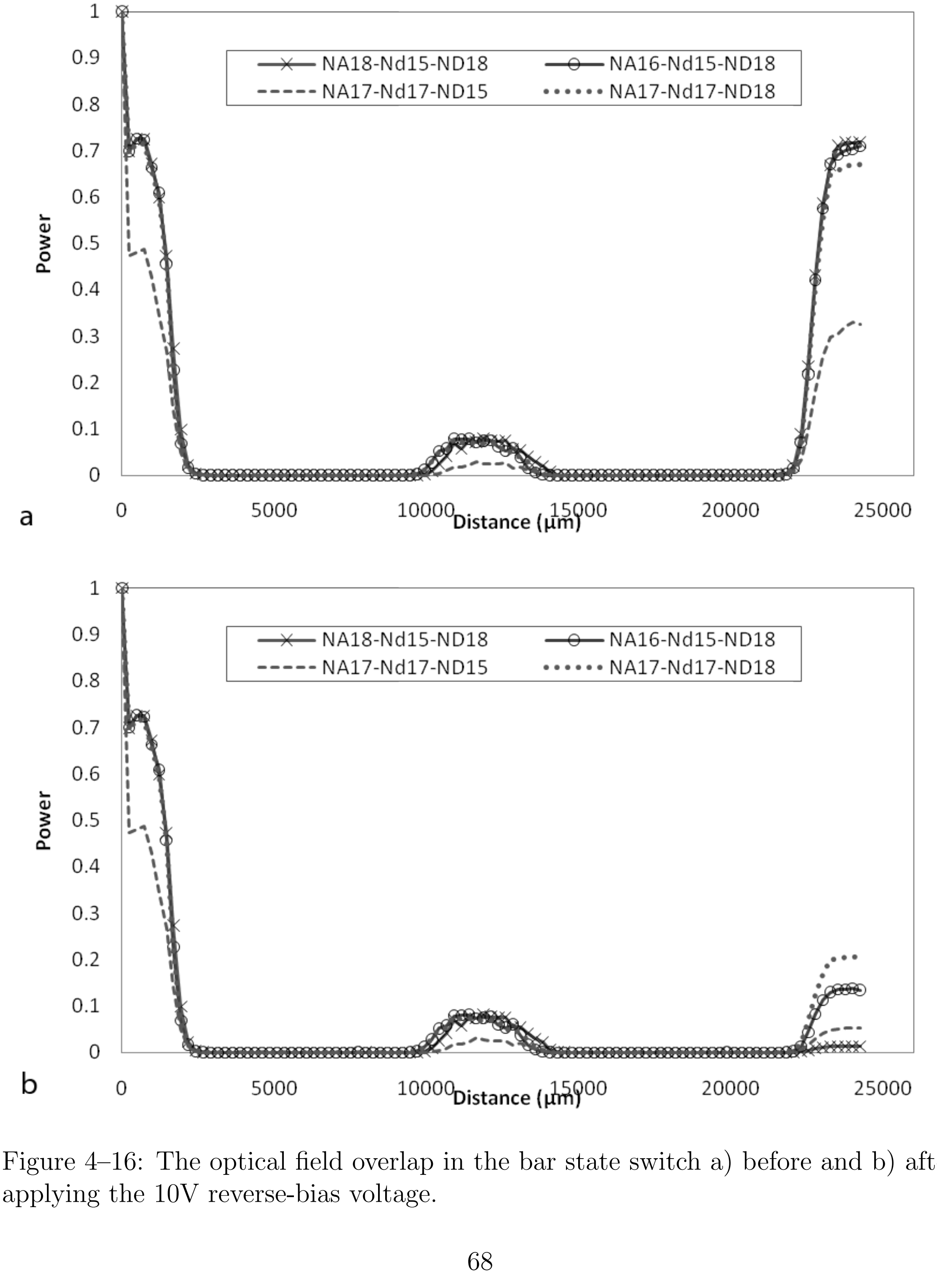

Figure 4–16: The optical field overlap in the bar state switch a) before and b) after applying the 10V reverse-bias voltage.

along the thickness of the waveguide, shown in Figure 4-17. In this figure, the one-dimension modeling of the structure in the y (thickness) direction has been carried out using the software developed by Snider [45]. The conduction band energy becomes negative in the lower cladding region of structures with 10^{18} cm^{-3} doped claddings while in the 10^{15} cm^{-3} doped lading, it is still positive. This translates into much more concentration of electrons and therefore higher carrier-related index reduction in the lower cladding. The lower refractive index brings about a higher confinement inside the core region.

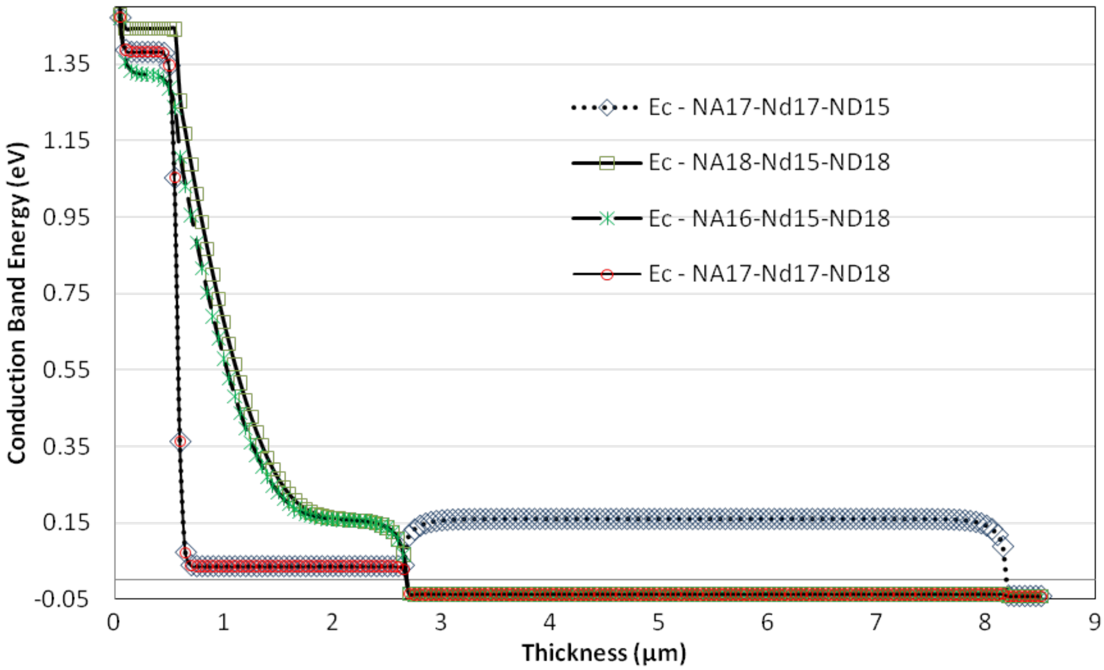

Figure 4–17: The conduction band energy of the structure versus the depth from the surface.

In Figure 4-18, the overlap power changes versus beam traveling distance in $Al_xGa_{1-x}As$ claddings with x values of 0.1 and 0.15 are compared against that of a

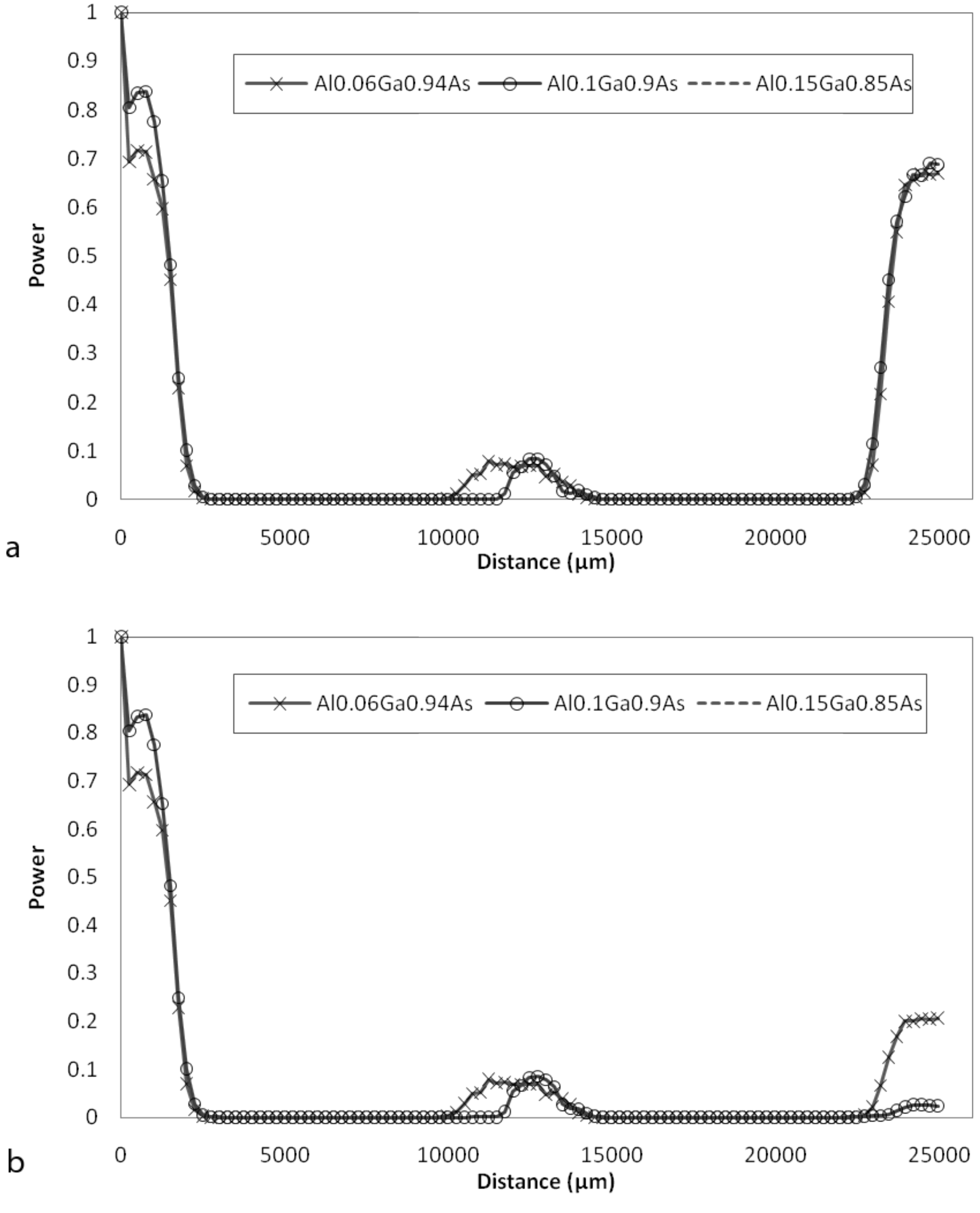

Figure 4–18: The optical field overlap in the bar state switch a) before and b) after applying the 10V reverse-bias voltage.

typical structure with x value of 0.06. As expected, the overlap power is generally higher in the optical switches comprising of claddings with higher Al contents (i.e. lower refractive indices) which result in higher light confinement in their core region.

4.6 Analysis of the Waveguide Performance

The insertion loss, i.e. the loss of signal power, in the waveguides is defined as,

$$Insertion.Loss(dB) = 10\log_{10}\left(\frac{P_{out}}{P_{in}}\right) \tag{4.9}$$

where P_{out} and P_{in} are the output and input power. Table 4-2 presents a summary of insertion losses in waveguides of different doping profiles in their bar- and cross-states.

Table 4–2: The calculated insertion loss for different switching materials

X	Upper Clad N_A (cm^{-3})	Core N_d (cm^{-3})	Lower Clad N_D (cm^{-3})	Insertion- bar state	Loss (0V) cross state	Insertion- bar state	Loss (-10V) cross state
0.06	10^{18}	10^{15}	10^{18}	-0.12	-15.67	-17.3	-0.08
0.06	10^{16}	10^{15}	10^{18}	-0.06	-18.55	-7.16	-0.93
0.06	10^{17}	10^{17}	10^{18}	-0.14	-14.84	-5.25	-1.54
0.06	10^{17}	10^{17}	10^{15}	-1.63	-5.05	-9.49	-0.52
0.10	10^{18}	10^{18}	10^{18}	-0.68	-8.39	-15.28	-0.13
0.15	10^{18}	10^{16}	10^{18}	-2.16	-4.07	-6.01	-1.25

The maximum transmittance of a modulator is almost always less than unity because of losses that can arise from reflection, absorption and scattering. Additionally, the minimum transmittance is not exactly zero as a result of misalignments of the propagation direction and polarization directions relative to the crystal axes and the polarizers [14]. The extinction ratio is defined as the ratio between the maximum and minimum transmittance,

$$Ex.R.(dB) = 10\log_{10}\left(\frac{P_{low}}{P_{high}}\right) \tag{4.10}$$

where P_{high} and P_{low} are the highest and lowest output powers in each state. The calculated extinction ratios for different doping profiles are summarized in Table 4-3.

Table 4–3: The extinction ratio of the waveguide with different doping profiles

X	Upper Clad N_A (cm^{-3})	Core N_d (cm^{-3})	Lower Clad N_D (cm^{-3})	Extinction bar state	Ratio (dB) cross state
0.06	10^{18}	10^{15}	10^{18}	-15.55	-17.22
0.06	10^{16}	10^{15}	10^{18}	-18.49	-6.23
0.06	10^{17}	10^{17}	10^{18}	-14.7	-3.71
0.06	10^{17}	10^{17}	10^{15}	-3.42	-8.97
0.10	10^{18}	10^{18}	10^{18}	-7.71	-15.15
0.15	10^{18}	10^{16}	10^{18}	-1.91	-4.76

According to Table 4-3, the switch with the $N_A18 - N_d15 - N_D18$ profile shows the best performance in terms of extinction ratio followed by $N_A16 - N_d15 - N_D18$. Waveguide structures made of $Al_xGa_{1-x}As$ claddings with x values higher than 0.06 were found to suffer from low extinction ratios. In general, waveguides with higher extinction ratios (more negative numbers, i.e. $< -40dB$) are preferred in the telecommunication switching applications. Minimum operation temperature, voltage and/or thickness wedge can result in higher extinction ratios [2] and might be employed to further improve the performance.

4.7 Summary

The optimum Al content of $AlGaAs$ claddings was found to be 0.06 $at\%$. Although, higher Al content in claddings can lead to higher confinements, it creates a switch with low extinction ratios. An optical switch with the 10^{18} cm^{-3} doped $Al_{0.06}Ga_{0.94}As$ upper cladding, 10^{15} cm^{-3} doped $GaAs$ core, and 10^{18} cm^{-3} doped $Al_{0.06}Ga_{0.94}As$ lower cladding was found to yield the best results in terms of power efficiency, extinction ratio and switch dimensions.

CHAPTER 5
Conclusion

In this work, the effect of doping on the performance of the Mach-Zehnder optical switches with a double heterostructure was simulated. First of all, the static permittivity and electro-optic coefficient of the materials of interest at the working wavelength (1550nm), and for different alloy compositions as well as doping levels were modeled. Secondly, the electric field-related effects (the Pockels and electro-refractive effect) as well as the carrier-related effects (the band filling and plasma effect) were evaluated and the overall change in the refractive index due to these mechanisms was determined. The optical switch device was finally designed based on the most efficient doping profiles and its performance in each condition was evaluated by beam propagation software.

The best combination of the extinction ratio, power efficiency and overall switch dimensions was found in an optical switch with the 10^{18} cm^{-3}-doped $Al_{0.06}Ga_{0.94}As$-upper-cladding, 10^{15} cm^{-3}-doped $GaAs$-core and 10^{18} cm^{-3}-doped $Al_{0.06}Ga_{0.94}As$-lower-cladding. Devices with claddings made of aluminum gallium arsenide with higher Al contents were found to lack the extinction ratios needed for telecommunication switching applications.

The $V_{\pi}.L$ values in these design ranged from 5.15 to 14 V-mm. These values were more promising than 1.4 V-cm found by Feng et al [46] for a 1 mm long SOI (silicon on insulator) device at 6V. Chen et al. [47] found a $V_\pi.L$ value of 2 V-mm in a device made of $AlGaInAs$ quantum wells. Ushigome et al. [48] found this value as 1.2 V-mm in a structure made of $InGaAs/InAlAs$ five layer asymmetric coupled quantum wells, with half-wave voltage of 2.3 V. Hence, using quantum wells in the structure as well as moving towards $InGaAs/InAlAs$ multilayers can further decrease the $V_\pi.L$ value and in other words result in a more efficient phase modulation.

Previously, Menard and Kirk [6] developed a 2 × 2 integrated Fabry-Perot space switch based on $GaAs/AlGaAs$ planar waveguides. By utilizing the optimized doping profile found in this work in their design, an optimized refractive index modulation as a function of applied voltage can be expected that can lead to a better performance by the optical switch. A trade off has to be measured between the refractive index modulation amount and extra insertion loss which arises from the dopants.

References:

1. A. Tzanakaki, et al., “Optical add/drop multiplexers and optical cross-connects for wavelength routed networks” in Transparent Optical Networks, 2003. Proceedings of 2003 5th International Conference on, 2003, pp. 41-46 vol.1.
2. T. S. El-Bawab, Optical switching. New York, N.Y.: Springer, 2006.
3. R. Izmailov, et al., “Hybrid hierarchical optical networks” Communications Magazine, IEEE, vol. 40, pp. 88-94, 2002.
4. M. Renaud, et al., “Semiconductor optical space switches” Selected Topics in Quantum Electronics, IEEE Journal of, vol. 2, pp. 277-288, 1996.
5. T. S. A. El-Bawab, Optical switching. New York: Springer, 2006.
6. M. Mnard, “Integrated Fabry-Perot optical space switches” PhD, Electrical and Computer Engineering, McGill University, Montral.
7. G. I. Papadimitriou, et al., “Optical switching: switch fabrics, techniques, and architectures” Lightwave Technology, Journal of, vol. 21, pp. 384-405, 2003.
8. C. R. Doerr, et al., “Wavelength-division multiplexing cross connect in InP” Photonics Technology Letters, IEEE, vol. 10, pp. 117-119, 1998.
9. A. Y. a. P. Yeh, Optical waves in crystals: propagation and control of laser radiation. New York: Wiley, 2003.
10. M. Mnard, “Integrated Fabry-Perot optical space switches” PhD, Electrical and computer engineeing, McGill University, Montreal, 2009.
11. N. Chitica, et al., “Fabrication of tunable InP/air-gap Fabry-Perot cavities by selective etching of $InGaAs$ sacrificial layers” Physica Scripta, p. 131, 1999.

12. Feb 11, 2011). $http://www.citizendia.org/Lithium_niobate$.
13. N. Dagli, High-speed photonic devices: Taylor & Francis, 2007.
14. B. E. A. Saleh and M. C. Teich, Fundamentals of Photonics: John Wiley & Sons, Inc., 2007.
15. J. G. Mendoza-Alvarez, et al., “Analysis of depletion edge translation lightwave modulators” Lightwave Technology, Journal of, vol. 6, pp. 793-808, 1988.
16. J. H. Davies, The Physics of Low-dimensional Semiconductors. New York: Cambridge University Press, 2006.
17. E. F. Schubert, Light Emitting Diodes, 2 ed.: Cambridge University Press, 2006.
18. S. R. Marder, et al., “Design and synthesis of chromophores and polymers for electro-optic and photorefractive applications” Nature, vol. 388, pp. 845-851, 1997.
19. R. Dinu, et al., “Environmental Stress Testing of Electro-Optic Polymer Modulators” J. Lightwave Technol., vol. 27, pp. 1527-1532, 2009.
20. L. Eldada, “Polymer integrated optics: promise vs. practicality”.
21. C. T. DeRose, et al., “Pockels coefficient enhancement of poled electro-optic polymers with a hybrid organic-inorganic sol-gel cladding layer” Applied Physics Letters, vol. 89, p. 131102, 2006.
22. G. Hougham, et al., “Influence of Free Volume Change on the Relative Permittivity and Refractive Index in Fluoropolyimides” Macromolecules, vol. 29, pp. 3453-3456, 1996.

23. G. Hougham, et al., “Polarization Effects of Fluorine on the Relative Permittivity in Polyimides” Macromolecules, vol. 27, pp. 5964-5971, 1994.
24. H. Ma, et al., “Polymer-Based Optical Waveguides: Materials, Processing, and Devices” Advanced Materials, vol. 14, pp. 1339-1365, 2002.
25. D. Boese, et al., “Chain orientation and anisotropies in optical and dielectric properties in thin films of stiff polyimides” Journal of Polymer Science Part B: Polymer Physics, vol. 30, pp. 1321-1327, 1992.
26. S. Herminghaus, et al., “Large anisotropy in optical properties of thin polyimide films of poly(p-phenylene biphenyltetracarboximide)” Applied Physics Letters, vol. 59, pp. 1043-1045, 1991.
27. Polymers for Electronic and Photonic Applications. New York Academic Press, 1993.
28. V. Doushkina. (2010) Advantages of Polymer and Hybrid Glass-Polymer Optics. Photonics Spectra.
29. Y. Shi, et al., “Electro-optic polymer modulators with 0.8 V half-wave voltage” Applied Physics Letters, vol. 77, pp. 1-3, 2000.
30. B. E. A. Saleh and M. C. Teich, Fundamentals of Photonics: John Wiley & Sons, Inc., 2001.
31. S. Adachi, “Refractive indices of III–V compounds: Key properties of $InGaAsP$ relevant to device design” Journal of Applied Physics, vol. 53, pp. 5863-5869, 1982.

32. S. Adachi, “$GaAs$, $AlAs$, and $Al_xGa_{1-x}As$ @B: Material parameters for use in research and device applications” Journal of Applied Physics, vol. 58, pp. R1-R29, 1985.
33. S. Adachi and K. Oe, “Internal strain and photoelastic effects in $Ga_{1-x}Al_xAs/GaAs$ and $In_{1-x}Ga_xAs_yP_{1-y}/InP$ crystals” Journal of Applied Physics, vol. 54, pp. 6620-6627, 1983.
34. S. Adachi and K. Oe, “Linear electro-optic effects in zincblende-type semiconductors: Key properties of $InGaAsP$ relevant to device design” Journal of Applied Physics, vol. 56, pp. 74-80, 1984.
35. M. Glick, et al., “Linear electro-optic effect: Comparison of $GaAs/AlGaAs$ multi-quantum-well heterostructures with an $AlGaAs$ solid solution at 1.1523 mu m” Journal of Applied Physics, vol. 63, pp. 5877-5879, 1988.
36. B. J. Baliga, “Material Properties and Transport Physics” in Fundamentals of Power Semiconductor Devices, ed: Springer US, 2008, pp. 23-89.
37. E. Rosencher and B. Vinter, Optoelectronics: Cambridge University Press, 2002.
38. J. F. Vinchant, et al., “$InP/GaInAsP$ guided-wave phase modulators based on carrier-induced effects: theory and experiment” Lightwave Technology, Journal of, vol. 10, pp. 63-70, 1992.
39. J. S. Barton, “The Integration of Mach-Zehnder Modulators with Sampled Grating DBR Lasers” UCSB, 2004.
40. Y. Bourbin, et al., “Electro-optical modulators using novel buried waveguides in $GaInAsP/InP$ material” Electronics Letters, vol. 24, pp. 221-223, 1988.

41. M.-S. Kwon, et al., “Fabrication of an integrated optical filter using a large-core multimode waveguide vertically coupled to a single-mode waveguide” Opt. Express, vol. 11, pp. 2211-2216, 2003.

42. R. R. Tummala, Fundamentals of microsystems packaging: McGraw-Hill 2001.

43. Y.-H. So, et al., “Benzocyclobutene-Based Polymers for Microelectronic Applications” in Polymers for Microelectronics and Nanoelectronics. vol. 874, ed: American Chemical Society, 2004, pp. 279-293.

44. H. Jin, et al., “General analysis of electrodes in integrated-optics electrooptic devices” Quantum Electronics, IEEE Journal of, vol. 27, pp. 243-251, 1991.

45. G. Snider. (2011, 1D Poisson/Schrodinger software at: http://www.nd.edu/ gsnider/.

46. N.-N. Feng, et al., “High speed carrier-depletion modulators with 1.4V-cm V_πL integrated on 0.25μm silicon-on-insulator waveguides” Opt. Express, vol. 18, pp. 7994-7999, 2010.

47. H.-W. Chen, et al., “High speed hybrid silicon evanescent Mach-Zehnder modulator and switch” Opt. Express, vol. 16, pp. 20571-20576, 2008.

48. M. Ushigome, et al., “Low voltage mach-zehnder modulator with $InGaAs/InAlAs$ five layer asymmetric coupled quantum wells” in LEOS Annual Meeting Conference Proceedings, 2009. LEOS ’09. IEEE, 2009, pp. 434-435.